
Multi-frequency mapping of the S255IR region at a wavelength of 1 mm

© 2025 E. A. Mikheeva,^{1,*} S. V. Kalenskii,^{1,†}
 S.-Y. Liu,² A. M. Sobolev,^{3,4} and S. Kurtz⁵

¹Lebedev Physical Institute, Russian Academy of Sciences, Aerospace Center, Moscow, Russia

²Institute of Astronomy and Astrophysics, Academia Sinica, Taipei, Taiwan

³Xinjiang Astronomical Observatory, Chinese Academy of Sciences, Urumqi, China

⁴Ural Federal University, Yekaterinburg, Russia

⁵Instituto de Radioastronomía y Astrofísica,

Universidad Nacional Autónoma de México, Morelia, Mexico

The results of interferometric observations of the star-forming region S255IR in the frequency range 210–250 GHz are presented. The observations were carried out with the antenna array SMA (Hawaii, USA). We present the spectra of molecular cores SMA1 and SMA2 and the maps of the region for a large number of various molecular lines. In total, fifty-three molecules were detected, including complex organic molecules (COMs) such as CH₃CHO, CH₃CN, CH₃CH₂CN, and many others. Typical rotational temperatures in the hot core SMA1 fall in the range 100–200 K. Optical depths in the lines of methanol and some other molecules in the cores SMA1 and SMA2 were estimated. In SMA1, the optical depth of one of the strongest methanol lines, 5₋₁ – 4₋₁E, proved to be 23.8 ± 1.5 . Based on this value, one can assume that the lines of other oxygen-containing COMs, such as CH₃OCHO, CH₃OCH₃, CH₃CH₂OH, which are typically much less abundant in hot cores than methanol, are optically thin in SMA1.

Most of the detected molecules can be roughly divided into two groups. The molecules of the first group emit exclusively toward the hot core SMA1, while some or all lines of the molecules of the second group, in addition to SMA1, can be seen toward a ring-like structure to the west of SMA1. This structure is most likely associated with the walls of a cavity formed by high-velocity outflows driven by young stellar objects (YSOs) in molecular cores SMA1, SMA2, and possibly SMA3. The gas temperature and density in the cavity walls were estimated using methanol lines. The temperature was found to be about 50–60 K, and the density about 10^7 – 10^8 cm^{−3}. The column density of methanol near the brightness peaks in the lines of this molecule is about 5×10^{15} cm^{−2}. The column densities of other COMs in the ring-like structure will be determined in future studies with increased sensitivity achieved by spectral line stacking.

Keywords: interstellar medium: star formation, molecular clouds, astrochemistry

* e.mikheeva@lebedev.ru

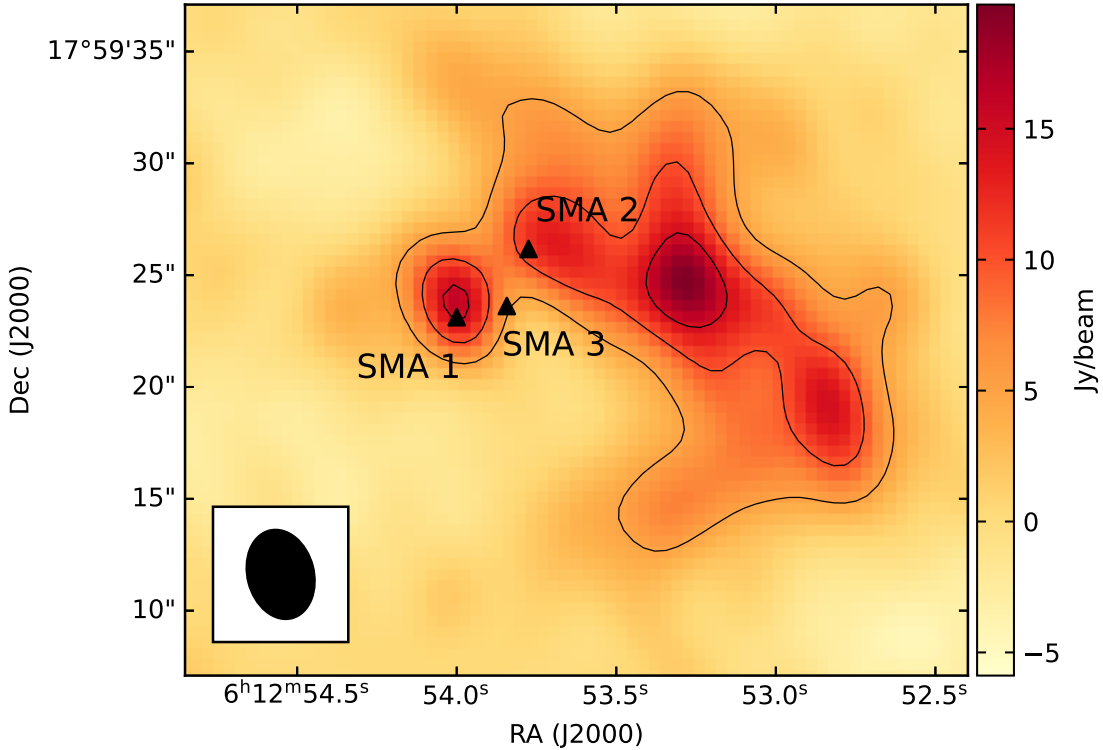
† kalensky@asc.rssi.ru

I. INTRODUCTION

The subject of this study is the high-mass star-forming region S255IR, located at a distance of 1.78 kpc from the Sun ([1]) in the direction near the Galactic anticenter ($l=192^\circ$). It is the middle region in the chain of star-forming regions S255N, S255IR, and S255S. This chain is hosted by the same molecular cloud, sandwiched between the HII regions S255 and S257, which are part of the S254–S258 complex of ionized hydrogen regions. S255IR is the most evolved among the three regions in the chain; it contains three radio continuum sources [2]; [3]; [4] associated with H_2O masers, as well as with Class II CH_3OH masers [5]; [6], which, in turn, indicate the presence of massive young stellar objects (MYSOs) in S255IR. Using MSX and IRAS data, Minier et al. [7] estimated bolometric luminosity of S255IR (G192.60–MM2 in their notation). Assuming a distance of 2.6 kpc they obtained $L_{bol} = 5.1 \times 10^4 L_\odot$, which yields L_{bol} recalculated for a distance of 1.78 kpc approximately equal to $2.4 \times 10^4 L_\odot$.

The region contains numerous infrared sources, the most prominent of which are NIRS1, whose nature is not entirely clear [8]; [9], and a young stellar object (YSO) NIRS3 with a mass of about $20 M_\odot$ and a bolometric luminosity of $\sim (2 - 4) \times 10^4 L_\odot$ ([4]; [10], [11]). These objects coincide with the dense cores SMA3 and SMA1, respectively (e.g., [9])(see Fig. 1). In the mid-infrared range, NIRS3 appears as a disk seen almost edge-on ([12]). The axis of the large-scale ($\sim 1'$, which corresponds to a projected distance of ~ 0.5 pc) bipolar outflow, observed in CO and other molecular lines, is almost perpendicular to the disk ([11]; [13]).

Figure 1. Map of the S255IR region in the $5_0 - 4_0 A^+$ methanol line at a frequency of 241791.367 MHz. Triangular markers indicate the dense cores SMA1 (coincident with NIRS3), SMA2, and SMA3 (coincident with NIRS1)



Particular interest in the S255IR region arose after a Class II methanol maser (MMII) flare at

6.7 GHz was detected in 2015 towards the NIRS3 source ([14]). Since MMII pumping is achieved by infrared radiation, immediately after the detection of this flare, observations of S255IR were carried out in the H ($1.65\text{ }\mu\text{m}$) and Ks ($2.16\text{ }\mu\text{m}$) bands, which showed an increase in brightness of $\Delta\text{H} \sim 3.5$ magnitudes and $\Delta\text{Ks} \sim 2.5$ magnitudes ([15]; [16]). Furthermore, the brightness of the infrared radiation toward the cavities, which were formed by the bipolar outflow from the protostar and scatter its radiation, increased noticeably. These facts indicate an outburst due to episodic accretion. Observations of the light echo propagation from the outburst between November 2015 and February 2016 established that the outburst began around mid-June 2015 ([16]). The results of near-infrared monitoring of the outburst are presented in [17]. The outburst reached its maximum intensity in December 2015, after which a gradual decline began. By March 2019, the infrared emission intensity had returned to its pre-outburst level.

Various authors ([1], [4]; [11]), based on observational data of water vapor masers and shock waves, have reported at least three outbursts preceding the 2015 event, with estimated ages of ~ 7000 years, ~ 1000 years, and ≤ 130 years. Apparently, outbursts in S255IR SMA1 occur episodically, similar to accretion outbursts in low-mass protostars. In the case of massive primordial star formation, episodic accretion bursts may play an important role in regulating the ionizing radiation emitted from the embedded massive star and providing a mechanism of prolonging accretion into the UCHII phase of massive star birth (see [1] and references therein).

The next most intense source of submillimeter continuum in this region is the SMA2 core ([4], [10]), located approximately $4''$ northwest of SMA1. This core is also observed in lines of ammonia, methanol, and other molecules, and is likely the center of a bipolar outflow ([9], [18]).

The SMA3 core is associated with the NIRS1 source. As a result of near-infrared polarimetric observations, Simpson et al. ([8]) discovered an S-shaped curved outflow oriented north-south and suggested that NIRS1 is a part of a binary system. However, Zinchenko et al. [9] were unable to detect this outflow in the 3–2 CO line, possibly because the outflow lies close to the plane of the sky.

The 2015 outburst attracted significant research attention to the S255IR region. Numerous observations of the area were conducted across various spectral ranges, both in continuum and in lines of different molecules ([10], [11], [9], [18], [19], [20] etc). Primarily, lines of simple molecules—CO, CS, SiO, CCH, NH₃, etc.—were observed and analyzed. Using data from the observations of these molecular lines, it was possible to estimate the main parameters of the SMA1 and SMA2 cores. It was found that SMA1 is a hot core with a temperature of about 170 K ([11]), while for the SMA2 core the same study derived a temperature of 50 K. Liu et al. (2018) [21] detected lines of several complex organic molecules (COMs)—CH₃CHO, CH₃OCHO, CH₃CH₂OH, and others—in the spectrum of SMA1, but their analysis was limited to the CH₃CN lines.

Thus, relatively little is known about complex molecules in the S255IR region. Therefore, in 2020, we conducted observations of the S255IR region with the SMA interferometric array covering a wide frequency band of 210–250 GHz. This resulted in a dataset suitable for studying a large number of molecules. The aim of this work is to study the spatial distribution of various molecules—primarily COMs—in the S255IR region, as well as to conduct a comprehensive investigation of the molecular composition of various objects in this area. This paper presents maps of the emission from COM lines, as well as from lines of some simple molecules¹. Furthermore, beam-averaged column densities and rotational temperatures of the molecules, derived using analytical methods assuming local thermodynamic equilibrium (LTE) in the source, are provided. More complete results of the spectral surveys, including non-LTE modeling results, will be presented in a separate paper.

¹ A map in a line of a simple molecule is provided if no maps for this molecule's lines could be found in the literature.

II. OBSERVATIONS AND DATA CALIBRATION

The S255IR region was observed on October 6, 2020, using the SMA Interferometric Array, consisting of eight six-meter telescopes located on the mountain Mauna Kea, Hawaii. The array was configured in a compact configuration, providing a spatial resolution of approximately $4''$ in the frequency range in which the observations were conducted. The 230 GHz (Rx A) and 240 GHz (Rx B) receivers were used, each receiving a single polarization plane; the planes are mutually orthogonal.

The backend of each receiver was a correlator in 12 GHz Dual Rx mode, providing two 12-GHz bands separated by an 8-GHz window. As a result, the Rx A receiver covered the 210–222 and 231–243 GHz frequency bands, and the Rx B, the 218–230 GHz and 238–250 GHz bands. Each band, in turn, was divided into six 2.28-GHz spectral windows with overlapping edges. The spectrometer resolution was 140 kHz, but it was smoothed during the data reduction to 1.117 MHz, which corresponds to a radial velocity resolution of 1.4 km/s at 240 GHz.

After observations the resulting array of visibility functions was converted at the radio telescope's Data Center to the Measurement Set format. This format is used for data reduction with the CASA software package, designed for processing radio interferometric data. The conversion was performed using the `pyuvdata` package [22], [23]; just at this stage the data were smoothed to a resolution of 1.117 MHz. Calibration and imaging were performed at the Astro Space Center of the Lebedev Physical Institute using the CASA package. First, the visibility functions were calibrated according to the SMA2 antenna array calibration manual (https://lweb.cfa.harvard.edu/rtdc/SMAdata/process/tutorials/sma_in_casaTutorial.html). Bandpass calibration was performed using the quasar 3C84. Point sources 0423–013 and 0510+180 were used as phase calibrators. Flux calibration was carried out using the solar system objects Vesta and Uranus.

Using the CASA task `split`, the array of calibrated visibility functions was split into 24 parts, each corresponding to one spectral window. From each spectral window, the continuum was subtracted using the task `uvcontsub`. As a result, we obtained a dataset of calibrated continuum-free visibilities, which were further used to construct maps of S255IR in various molecular lines and spectra of this region in different directions.

A. Map Construction Procedure

The map construction process was as follows. First, using the task `tclean` in non-iterative mode (`niter=0`), a spectral cube of 2048 channels was constructed for each spectral window, where each channel represents an image of the source at a specific frequency, convolved with the array beam («dirty»map). For deconvolution, a square patch of sky centered at R.A. = $6^h12^m53.800^s$, DEC = $+17^\circ59'22.09''$ (J2000) and 60 arcseconds in size was clipped from the spectral cube. This region includes NIRS1, NIRS3, and their environments. Subsequent cleaning was done in two stages. First, an initial, relatively rough deconvolution (cleaning of maps) was performed. This cleaning was performed using task `tclean` in non-interactive mode using a mask of dimensions $22'' \times 13''$ in right ascension and declination and was stopped when the standard deviation of the noise in the residual images stabilized. For quick viewing of the residual images, the `CARTA`² [24] software was used. Second, a spectrum for the total observed frequency range was constructed. During the construction of this spectrum, the radiation intensity in each channel was averaged over the region, centered in the direction $06^h12^m53.62^s, 17^\circ59'22.2''$ (J2000) and having dimensions $27'' \times 23''$, respectively, in right ascension and declination. This region includes all sources visible at this stage; thus, the

² Cube Analysis and Rendering Tool for Astronomy, <https://cartavis.org/>

spectrum was a net spectrum of SMA1, SMA2, and their environments. On this spectrum, using the catalog of spectral lines discovered in space³. by F. Lovas, lines of 27 molecules were identified, and *preliminary* maps were constructed for them.

Based on these preliminary maps, spectral lines were selected for further mapping. A list of these lines is given in Table IV. Most of selected lines arise from the molecules for which no detection in S255IR have been published. To construct the images, the continuum-free visibility functions in narrow spectral ranges around the line frequencies were transformed into spectral subcubes $60'' \times 60''$ in RA and DEC, which were interactively cleaned with natural weighting. Using these subcubes, both channel maps and line integrated intensity maps were constructed. The pixel sizes are $0.5'' \times 0.5''$. To eliminate edge effects, the maps were cropped at the edges to a size of $50'' \times 50''$.

To create the maps, Python programs were written using the «aply», «numpy», «matplotlib», and «astropy» libraries.

The clean beam size decreases with increasing frequency from $4.3'' \times 3.3''$ at 209.4 GHz to $3.8'' \times 2.9''$ at 249.7 GHz, respectively.

B. Construction of SMA1 and SMA2 Spectra

The spectra of SMA1 and SMA2 were constructed as follows. A region of $15'' \times 12''$ around SMA1 was selected for cleaning, which contains the strongest sidelobes of the synthesized beam, as well as the SMA2 and SMA3 cores. In each of the 24 continuum-free spectral windows, this region was cleaned non-interactively, constructing spectral cubes. After 20,000 iterations, cleaning was stopped, and the spectrum of the region was examined. If the contribution of spectral lines above 3 sigma was no longer detectable in the spectrum constructed from the residual image cubes, cleaning was stopped. Otherwise, the next cleaning step was performed, and so on. In practice, no spectral window required more than three steps.

In the spectral cubes thus cleaned, regions centered on SMA1 and SMA2 and $4'' \times 3''$ in size, which correspond to the angular sizes of the clean beam in declination and right ascension, were selected. Spectra were constructed for these regions, as shown in Figs. 2 and 3.

Numerous spectral lines were detected in the spectra of SMA1 and SMA2, the identification of which was carried out using the catalog of spectral lines discovered in space by F. Lovas (see section II A). However, many lines remained unidentified; their identification will be done in subsequent works during the analysis of the results of spectral surveys.

III. MAPS OF INTEGRATED LINE INTENSITIES AND CHANNEL MAPS

The spectra of SMA1 and SMA2 contain numerous spectral lines belonging to various molecules, ranging from simple two- and three-atomic species— ^{13}CO , C^{18}O , SiO , etc.—to complex organic molecules (COM)— CH_3OH , CH_3OCHO , CH_3CHO , $\text{CH}_3\text{CH}_2\text{OH}$ etc. (Table I). A list of the 53 detected molecules is given in table I. Many of them have already been observed in S255IR, and their maps have been presented and analyzed in a number of papers ([10], [11], [9], [21]). With some exceptions (see below), we did not consider the lines of these molecules. However, molecules were also discovered that have not been mapped in S255IR previously. Among these are COMs CH_3CHO , $\text{CH}_3\text{CH}_2\text{OH}$, $\text{CH}_3\text{CH}_2\text{CN}$, etc. We constructed maps in the lines of these molecules. In addition, the physical conditions necessary to produce emission in different transitions of the same molecule may be very different. Therefore, maps in different lines often do not coincide, and a set of

³ NIST Recommended Rest Frequencies for Observed Interstellar Molecular Microwave Transitions by Frank J. Lovas; <https://physics.nist.gov/cgi-bin/micro/table5/start.pl>

Figure 2. Spectrum toward SMA1

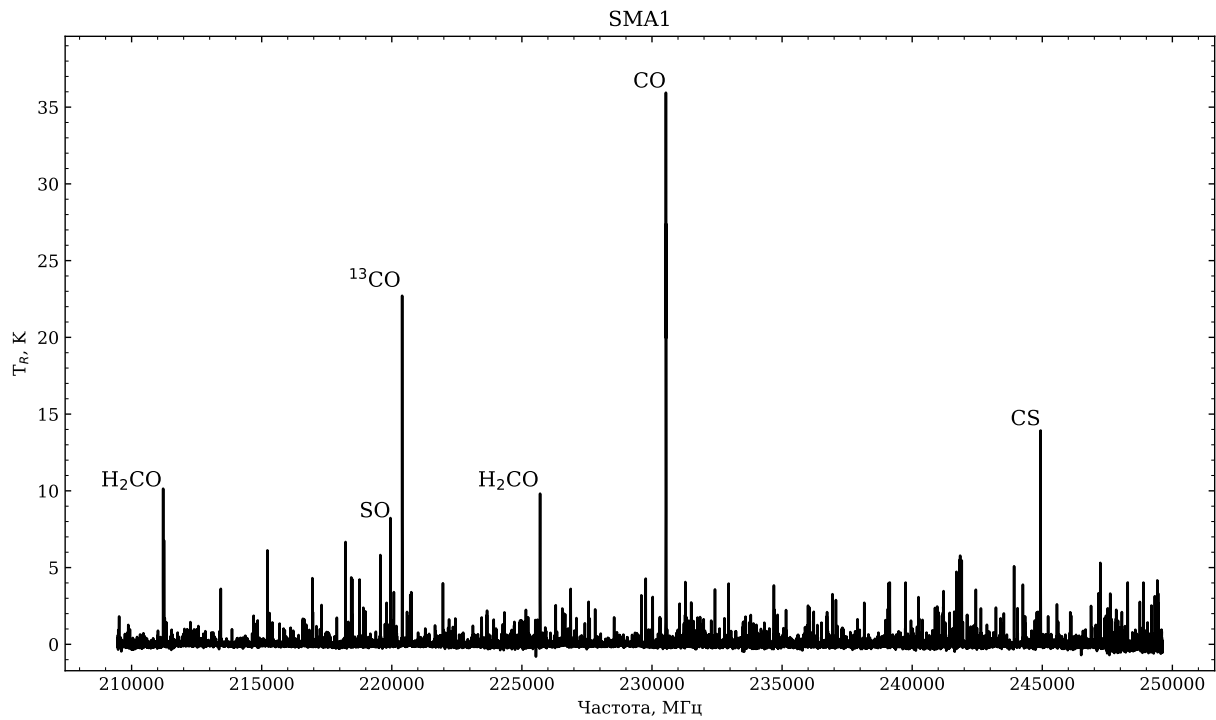
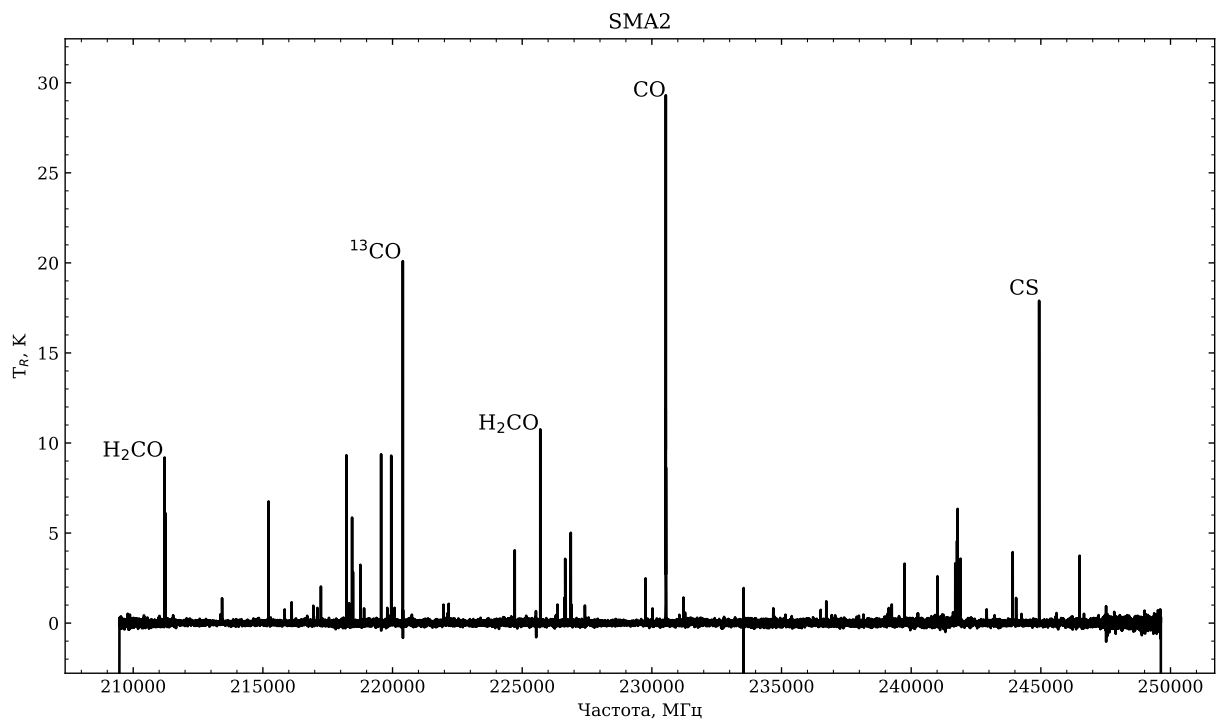


Figure 3. Spectrum toward SMA2



maps allows us to characterize the source more completely than a map in a single line. An example is the maps of S255IR in two different methanol lines (Fig. 7). Therefore, we also constructed maps of S255IR in the lines of methanol, methyl cyanide and some other molecules observed in this source earlier. The complete list of molecules for which maps were constructed in one or more lines is given in Table I, and the list of lines for which we constructed maps is presented in Table IV. The constructed maps are available online (<http://www.asc.rssi.ru/kalenskii/s255ir/s255ir.html>).

Table I. Molecules detected in the cores SMA1 and SMA2.

	SMA1	SMA2
Diatom	CO, C ¹⁸ O, C ¹⁷ O, ¹³ CO, CN, C ¹⁵ N, CS, C ³⁴ S, ¹³ CS, SiO, SO, ³³ SO, ³⁴ SO, S ¹⁸ O	CO, C ¹⁸ O, C ¹⁷ O, ¹³ CO, CN, CS, C ³⁴ S, ¹³ CS, ³⁴ SO, SO, SiO
Triatomic	DCN, H ₂ S, HDO, OCS, OC ³⁴ S, SO ₂ , ³⁴ SO ₂ , HCS ⁺	DCN, H ₂ S, OCS, SO ₂
Four-atom	H ₂ CO, H ₂ ¹³ CO, H ₂ CS, HNCO	H ₂ CO, H ₂ ¹³ CO, H ₂ CS, HNCO
Five-atom	CH ₂ CO, HCCCN, H ¹³ CCCN, HC ¹³ CCN, HCOOH, HCOOD, c-C ₃ H ₂ ?, CH ₂ NH, NH ₂ CN	c-C ₃ H ₂ , HCCCN
Six-atom	CH ₃ CN, ¹³ CH ₃ CN, CH ₃ ¹³ CN, CH ₃ OH, CH ₃ OD, ¹³ CH ₃ OH, CH ₃ SH?, NH ₂ CHO	CH ₃ OH, ¹³ CH ₃ OH, CH ₃ OD
Seven-atom	CH ₃ CHO, CH ₃ CCH, ¹³ CH ₃ CCH, CH ₃ NH ₂ , CH ₂ CHCN, c-C ₂ H ₄ O	CH ₃ CCH
Eight-atom	CH ₃ OCHO	
Nine-atom	CH ₃ CH ₂ CN, g-CH ₃ CH ₂ OH, t-CH ₃ CH ₂ OH, CH ₃ OCH ₃	

IV. RESULTS

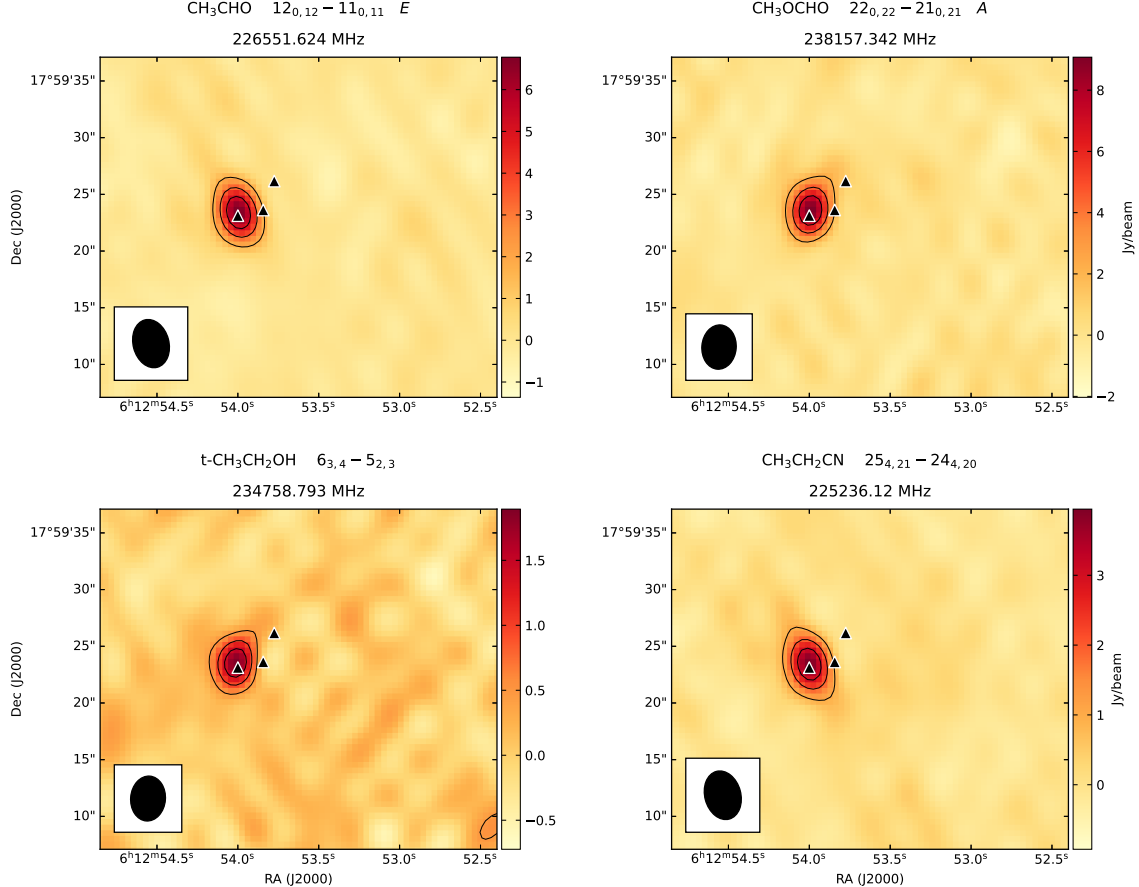
Based on the mapping results, all detected molecules can be divided into two large groups. The first group consists of HNCO, OCS, CH₃CHO, CH₂CO, CH₃OCHO, CH₃CN, and CH₃CH₂CN. In all lines of these molecules, emission is visible only toward SMA1 and the sources are not spatially resolved with our beam. As an example, Fig. 4 shows the integrated intensity maps of the lines of ethanal (CH₃CHO), methyl formate (CH₃OCHO), ethyl alcohol (CH₃CH₂OH), and ethyl cyanide (CH₃CH₂CN). The remaining maps in the lines of these molecules demonstrate a similar source structure, differing only in intensity.

Figure 5 demonstrates line profiles of the first group molecules. One can see that the LSR radial velocities are close to 5 km/s.

All or some lines of molecules of the second group emit not only in the SMA1 core, but also in other directions. Moreover, the emission of SMA1 is not necessarily the brightest, and in some cases is absent altogether.

One of the molecules of the second group is cyanogen (CN). We constructed maps in five hyperfine components of the 2–1 rotational transition. Fig. 6 shows the map of CN in the $J = 3/2 - 1/2$ $F = 5/2 - 3/2$ line. One can see that the source has a ring-shaped structure about 15" in diameter with several brightness peaks. One of the brightest peaks is located toward SMA2, while the emission brightness toward SMA1 is very low. The maps in the remaining detected $J = 3/2 - 1/2$ lines generally coincide with the map in the $J = 3/2 - 1/2$ $F = 5/2 - 3/2$ line. All images show the same ring-shaped structure with the brightest peak toward the SMA2 core and the second brightest component located approximately diametrically opposite SMA2. In contrast, the image

Figure 4. Maps in the $12_{0,12} - 11_{0,11} E$ ethanal (CH_3CHO) line, in the $22_{0,22} - 21_{0,21} A$ methyl formate (CH_3OCHO) line, in the $6_{3,4} - 5_{2,3}$ ethanol ($t\text{-CH}_3\text{CH}_2\text{OH}$) line, and in the $25_{4,21} - 24_{4,20}$ propionitrile ($\text{CH}_3\text{CH}_2\text{CN}$) line.

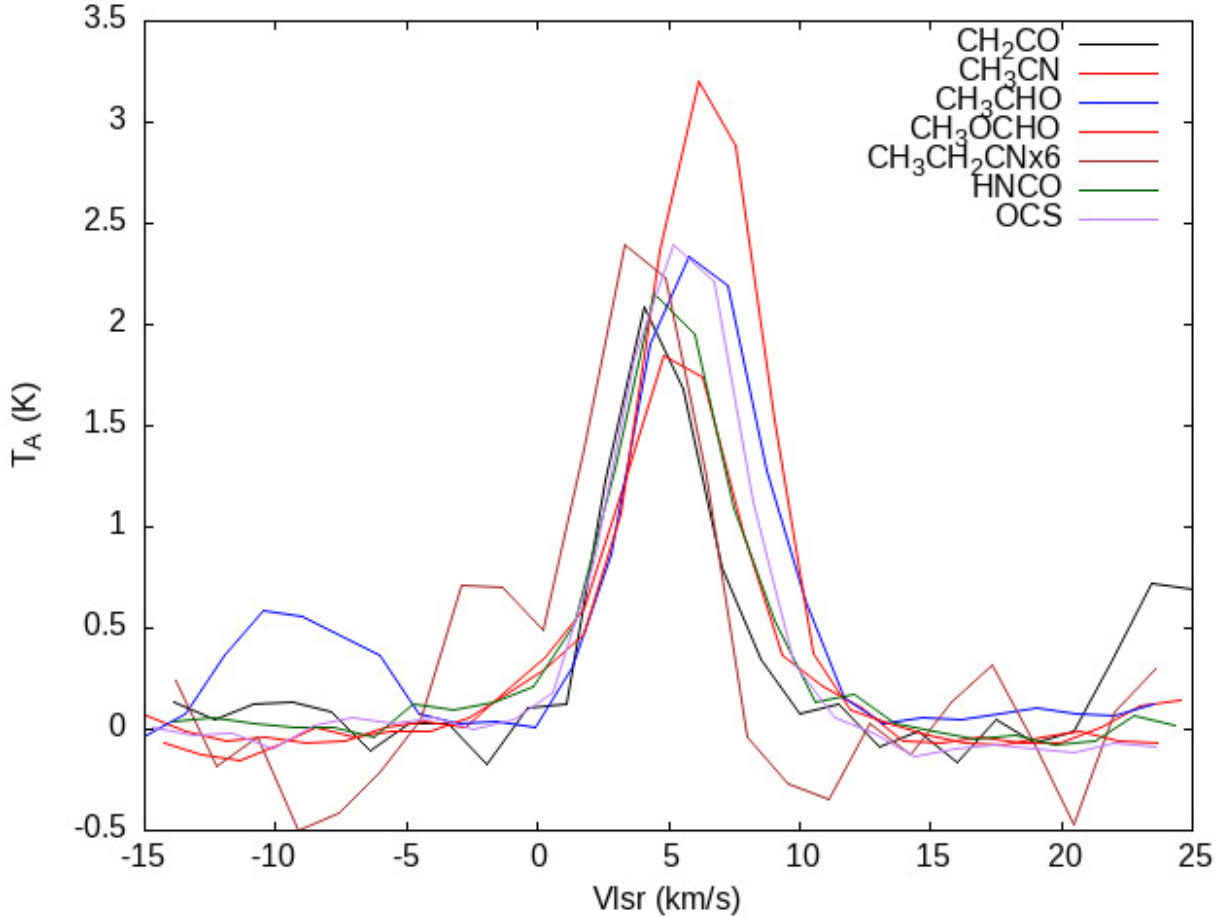


of the spectral feature at ≈ 226875 MHz, which is a blend of three hyperfine components of the $J = 5/2 - 3/2$ transition is noticeably different. The brightest region at 226875 MHz is extended and roughly coincides with the continuum structure discussed by e.g. Zinchenko et al. ([9]), and the peaks in the ring structure are two to three times less bright than this region.

The maps in the lines of some molecules resemble the CN ring with one or two breaks or a portion of this ring. For example, the image in the $5 - 4$ HCS^+ line at a frequency of 213360.650 MHz (Fig. 6) resembles this ring, but with the most noticeable break toward SMA1 and SMA3. The brightest peak approximately coincides with the bright peak on the CN maps, which is located diametrically opposite to SMA2. Another such molecule is CS. The image in the $5-4$ CS line at 244935.556 MHz (Fig. 6) has a ring shape with the brightest peaks toward SMA1 and SMA2 and a break at a distance of about $7''$ to the southwest of SMA1.

Images of the lines of other molecules— SiO and H_2S —do not show a ring-shaped structure. However, the regions emitting in the lines of these molecules are often located within the CN ring. Therefore, it is likely that these regions and the ring observed in the lines of CN and other molecules

Figure 5. Samples of spectral lines of the first group molecules. The figure shows the $11_{1,10} - 10_{1,9}$ CH₂CO line, the $12_4 - 11_4$ CH₃CN line, the $12_{0,12} - 11_{0,11}E$ CH₃CHO line, the $19_{3,17} - 18_{2,16}E$ CH₃OCHO line, the $24_{3,22} - 23_{3,21}$ CH₃CH₂CN line, the $10_{1,10} - 9_{1,9}$ HNCO line, and the 18 – 17 OCS line. Antenna temperature of the CH₃CH₂CN line is multiplied by six.

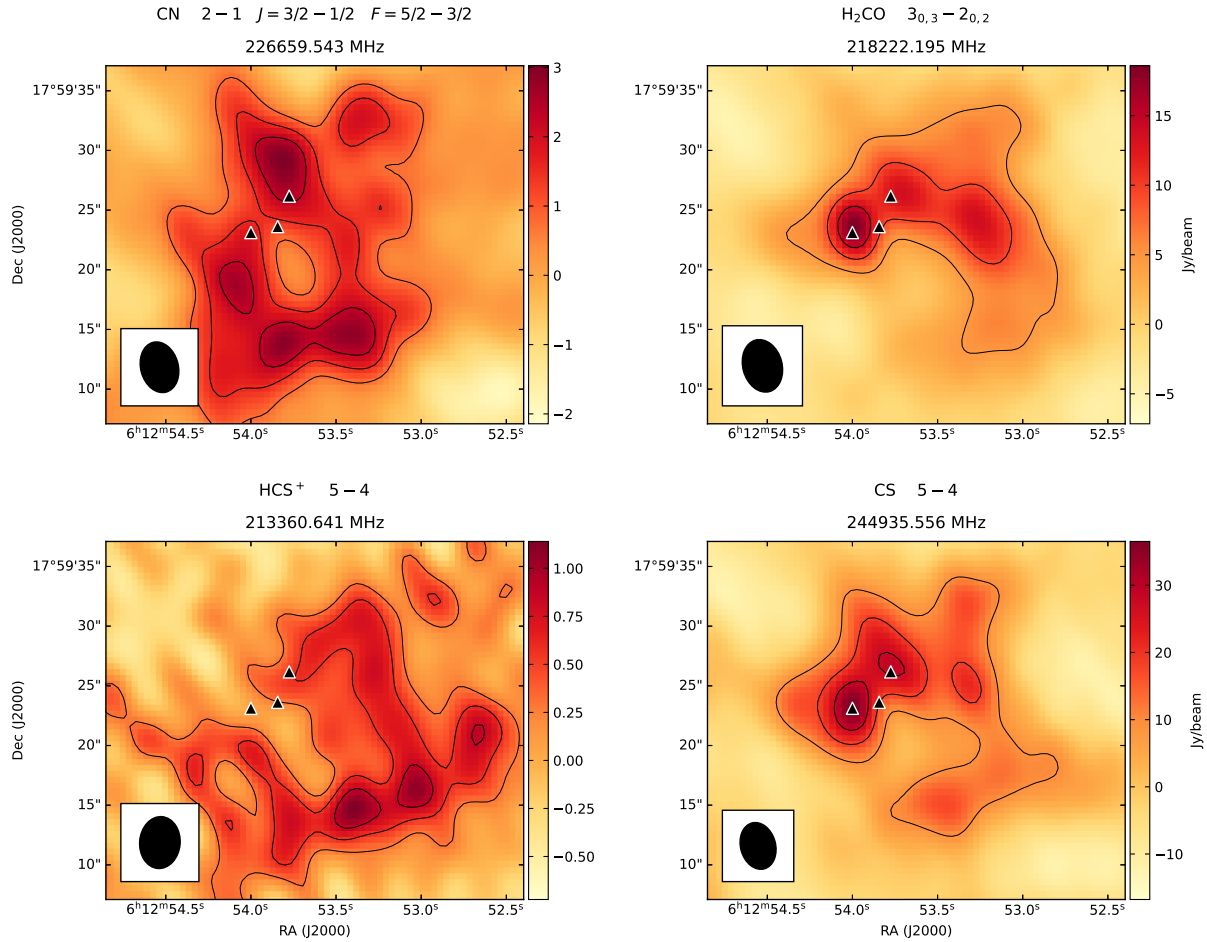


belong to the same physical structure, which will be discussed below.

A large number of maps have been constructed for various methanol lines, two of which are shown in Fig. 7. The emission in the lines with lower-level energy $E_{low} \gtrsim 50$ K is concentrated in the SMA1 direction (Fig. 7, left), while lines with $E_{low} < 50$ K show extended emission, as do the other Group II molecules (Fig. 7, right).

The low-level energies of all mapped lines of COMs CH₂CO, CH₃CHO, C₂H₅CN, CH₃CN, CH₃OCHO are above 50 K. It is possible that images of low-energy lines of these molecules would show a similar morphology to maps of molecules of the second group. It would be interesting to construct such maps and check whether these molecules are indeed present in gas phase only in the hot core SMA1. In addition, it is possible that the weak extended emission in the lines of at least some of the molecules of the first type (for example, H₂¹³CO) is not visible due to insufficient sensitivity. It's possible that some or even all of the molecules in the first group, like methanol, would show emission in regions other than SMA1 when observed with higher sensitivity. This issue will be investigated in future studies.

Figure 6. Upper row: maps of the integrated intensity of the $J = 3/2 - 1/2$ $F = 5/2 - 3/2$ CN line (left) and of the $3_{0,3} - 2_{0,2}$ H₂CO line (right). Lower row: maps of the 5–4 HCS⁺ line (left) and of the 5–4 CS line (right).

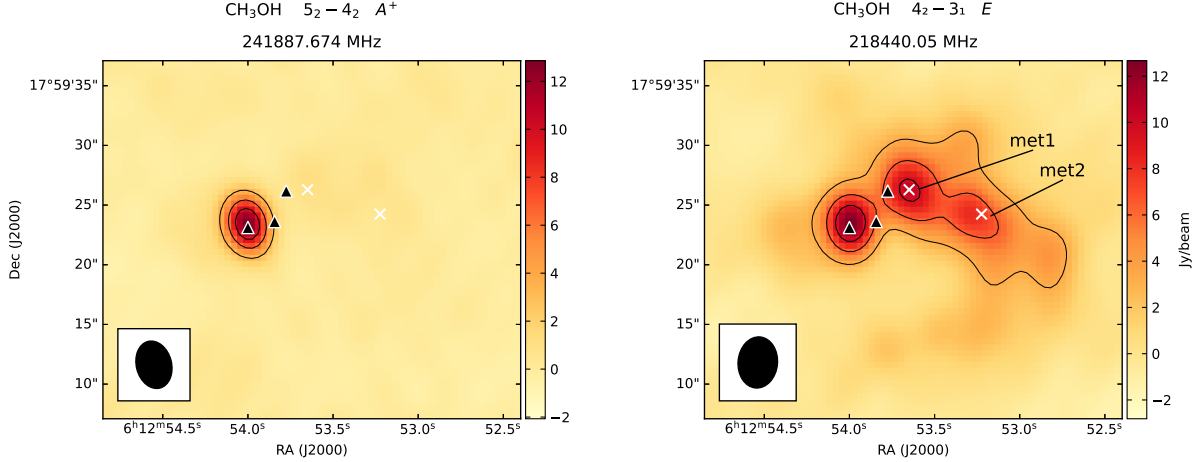


V. ROTATION DIAGRAMS

If four or more isolated lines of a molecule were detected in a single direction, we built a rotation diagram (RD) for this molecule. The RDs constructed for the molecules in the SMA1 direction are shown in Fig. 8. The scatter of points on the diagrams is fairly large, which in turn leads to fairly large uncertainties of both the rotational temperatures and the column densities of the molecules. This scatter may be caused by deviations from LTE; as for the optical depth, we do not believe that it could significantly affect the RDs built for the most of the detected COMs (see sect. VI). In addition to deviations from LTE, incorrect identification of lines may play a certain role.

Rotational temperatures (T_{rot}) for most molecules fall in the range 100–200 K. Higher T_{rot} values were obtained for HCOOH ($T_{rot} = 359$ K) and CH₃CN ($T_{rot} = 279$ K). Much lower value

Figure 7. Maps in methanol lines $5_2 - 4_2 A^+$ at 241887.674 MHz (left) and $4_2 - 3_1 E$ at 218440.05 MHz (right)



Molecule	Rotational temperature (K)	Column density (cm ⁻²)
H2CO	-649 15	NaN
HNCO	176 ± 15	$(7.4 \pm 0.8) \times 10^{14}$
HCOOH	359 ± 236	$(5.0 \pm 0.9) \times 10^{15}$
CH ₂ CO	184 ± 37	$(6 \pm 1) \times 10^{14}$
CH ₃ OH	168 ± 9	$(4.7 \pm 0.6) \times 10^{16}$
CH ₃ CN	279 ± 39	$(5.9 \pm 1.0) \times 10^{14}$
CH ₃ CCH	-435 ± 1343	NaN
CH ₃ CHO	108 ± 12	$(1.6 \pm 0.2) \times 10^{15}$
CH ₃ OCHO	32 ± 4	$(5 \pm 2) \times 10^{15}$
CH ₃ OCHO	266 ± 165	$(8 \pm 3) \times 10^{15}$
CH ₃ OCH ₃	123 ± 21	$(4.5 \pm 1.2) \times 10^{15}$
CH ₃ CH ₂ CN	36 ± 6	$(8.5 \pm 9.1) \times 10^{14}$
g-CH ₃ CH ₂ OH	179 ± 112	$(5.9 \pm 4.3) \times 10^{15}$
t-CH ₃ CH ₂ OH	125 ± 17	$(4.7 \pm 0.8) \times 10^{15}$

Table II. Rotational temperatures and column densities for the molecules detected toward SMA1

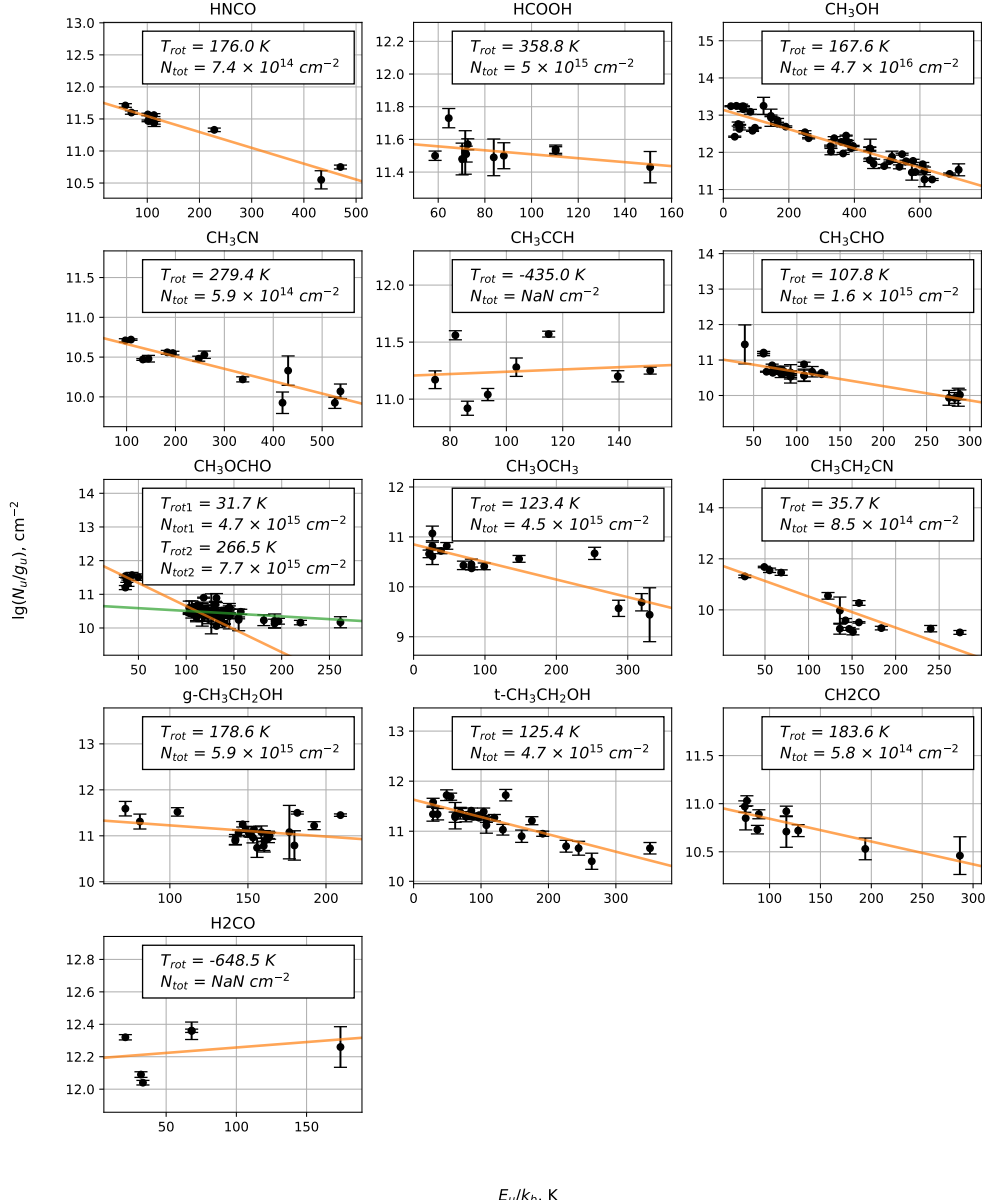
($T_{rot} = 36$ K) was found for CH₃CH₂CN⁴. The rotational temperature of formaldehyde, as well as of methylacetylene, which is considered a good thermometer of interstellar gas, was found to be negative. We believe that in the case of methylacetylene this may be caused by the absorption in the K=0 and 1 lines in a cold shell⁵; in the case of formaldehyde, in addition to the hypothetical shell, the absence of LTE and the large optical depth of the lines could have influenced the RD shape. The rotation diagram of CH₃OCHO is two-component: in the range of level energies 0 – 100 K, the rotational temperature is equal to 32 K⁶, and at level energies above 100 K its value is equal

⁴ This rotation diagram may be two-component, similar to the RD of methyl formate, but the number of points corresponding to $E_{up} \gtrsim 150$ K is not large enough to reliably establish the existence of a high-temperature component.

⁵ The results of modeling the CH₃CCH emission will be presented in the following paper.

⁶ Due to the absence of points in the range of level energies 70–100 K, the rotational temperature of the cold component is poorly determined and the obtained value is an upper limit.

Figure 8. Rotation diagrams built for the molecules detected toward SMA1



to 266 K.

Rotation diagrams were constructed for the hot core SMA1, as just here we found four or more lines for a number of molecules. In this object Zinchenko et al. [11] found a temperature of about 170 K. Liu et al [19] modelled CH₃CN emission in SMA1 and found that the temperature is higher than 400 K in the inner regions, gradually falling off to the temperature of $\gtrsim 100$ K toward the peripheral areas. Most of the molecules for which RDs were constructed belong to the first group, meaning that their emission was detected only in SMA1; the exceptions are methanol, methyl acetylene, and formaldehyde. Therefore, it is not surprising that in most cases the rotational temperature exceeds 100 K. However, the rotational temperature of ethyl cyanide is only 36 K, and the rotational temperature of the cold component of methyl formate is below 32 K. These facts indicate that the hot core is accompanied by cold gas, and the apparent angular dimensions of the cold source are smaller than the synthesized beam.

It should be noted that the presence of cold gas in SMA1 has been noted in previous studies. For example, Zinchenko et al. [11] constructed a rotation diagram for SO_2 in SMA1 based on observations with a spatial resolution of $2''$, which also turned out to be two-component. For low-energy levels, the rotational temperature was found to be 65 ± 11 K, and for high-energy levels, 146 ± 16 K. Zinchenko et al. explained the presence of the cold component by the contribution of a cloud surrounding the hot core. Moreover, based on the detection of a strong DCN emission near the center of the hot core, Zinchenko et al. [11] suggested a presence of a relatively cold (< 80 K) and rather massive clump there.

DCN is usually tracing pristine material and accretion inflows in it. Chen et al [25] detected infalling streamers toward a high-mass YSO G352.63, with the temperature of the infalling gas ~ 10 K. It is very probable that the same inflow exist in S255IR and its part is projected onto the central part of SMA1.

VI. OPTICAL DEPTHS OF ROTATIONAL LINES.

The optical depth of a rotational transition can be estimated when individual hyperfine components of this transition are observed. We detected several hyperfine components of the $2 - 1$ transition of CN radical. It turned out that some of them are either blended with other lines or are weak, and five components of this transition are suitable for determining the optical depth of the CN lines. Then, it was discovered that the $F = 1/2 - 1/2$ component at a frequency of 226663.685 MHz is anomalously strong. Perhaps it is blended with some unidentified line; the presence of hyperfine anomalies is also possible. We excluded this component and estimated the optical depth from the four remaining ones using the hfs method in the CLASS program. It turned out that the lines are optically thin, i.e., the optical depth of the most intense component does not exceed 0.1. However, it should be noted that such a procedure is incorrect in the case of hyperfine structure anomalies, and the obtained results should be used with caution.

The optical depth of molecular lines can also be estimated using substituted isotopologues. Suppose we observe the same transition of the primary and substituted isotopologues. In the case of equal and constant throughout the source excitation temperatures for both isotopologues the ratio of the line brightness temperatures is:

$$\frac{T_{br}^m}{T_{br}^s} = \frac{1 - e^{-\tau}}{1 - e^{-\tau/r}} \quad (1)$$

where T_{br}^m is the brightness temperature of the line of the main isotopologue, T_{br}^s is the brightness temperature of the line of the substituted isotopologue, τ is the optical depth of the line of the main isotopologue, r is the isotope ratio. Having determined the ratio T_{br}^m/T_{br}^s from observations, and adopting a standard isotope ratio, one can find the values of the optical depths of the main and substituted isotopologues. Using this method we estimated optical depths of some molecular lines in SMA1 and SMA2.

A. SMA1

To determine the optical depths of methanol and formaldehyde lines, ^{13}C isotopologues were used. The distance from the S255IR region to the Galactic center is 10.24 kpc; at this Galactocentric distance, the $^{12}\text{C}/^{13}\text{C}$ ratio in the ISM is 82, according to formula (5) from [26]. In the case of methanol, the brightness temperatures of the $5_{-1} - 4_{-1}$ E lines of the main isotopologue and $^{13}\text{CH}_3\text{OH}$ were compared. The optical depth of the $^{13}\text{CH}_3\text{OH}$ line proved to be 0.29, and that of the $^{12}\text{CH}_3\text{OH}$ line, 23.8 ± 1.5 .

It should be noted that in the hot gas the abundance of most COMs with rotational partition functions comparable to or exceeding the partition function of methanol is one and a half to three orders of magnitude lower than the abundance of methanol ([27], [28], [29], [30], [31]). In addition, the $5_{-1} - 4_{-1}E$ methanol line is one of the strongest among those we have detected; it is natural to assume that the characteristic values of the optical depths of other, weaker, methanol lines are lower than the optical depth of the $5_{-1} - 4_{-1}E$ line. Since the abundance of the remaining COMs in the hot gas is 30 or more times lower than the abundance of methanol, we assume that the emission in the COMs is optically thin and hence the optical depths do not affect the rotation diagrams.

In the case of formaldehyde, the $3_{1,2} - 2_{1,1}$ lines were used. The optical depth of the $H_2^{13}CO$ line was equal to 0.15, and that of the H_2CO was 12.3 ± 1.0 .

Optical depth of the $5-4$ CS line can be estimated using either the ^{13}CS isotopologue or the $C^{34}S$ isotopologue. We chose $C^{34}S$ because the $5-4$ ^{13}CS line is blended with some unidentified line. The ratio $^{32}S/^{34}S$ in the ISM is 22, according to [32]. Optical depth of the CS line proved to be 4.3 ± 0.5 , and the optical depth of the $C^{34}S$ line proved to be 0.2.

In the case of SO, the $N, J = 5, 6 - 4, 5$ transition of the main and ^{34}SO isotopologues were observed. Optical thickness of the line of the main isotopologue was found to be 2.70 ± 0.5 and that of the ^{34}SO isotopologue, 0.12.

We recorded three lines of carbonyl sulfide (OCS) in SMA1—18–17, 19–18 and 20–19. Optical depths of the lines 18–17 and 20–19 were estimated using the corresponding lines of the $OC^{34}S$ isotopologue. Optical depth of the 18–17 OCS line was 2.2 ± 1.2 , and that of the 20–19 OCS line, 1.4 ± 0.3 . Optical depths of the corresponding $OC^{34}S$ lines were 0.1 and 0.06, respectively.

B. SMA2

In SMA2, we could estimate the optical depths of the $5-4$ CS and $N, J = 5, 6 - 4, 5$ SO lines. The optical depth of the CS line was determined using the ^{13}CS and $C^{34}S$ isotopologues. In the first case, it was found to be equal to 6.4 ± 0.5 , and in the second, 3.2 ± 0.2 . Unlike in SMA1, in SMA2 the parameters of the $5-4$ lines of both the ^{13}CS isotopologue and the $C^{34}S$ isotopologue were determined reliably. The discrepancy between the obtained optical depth values may mean that either the $[13C/12C]$ ratio, or the $[34S/32S]$ ratio, or both of them differ from the accepted values. We used the average value of 4.8 ± 1.6 as the optical depth of the $5-4$ CS line.

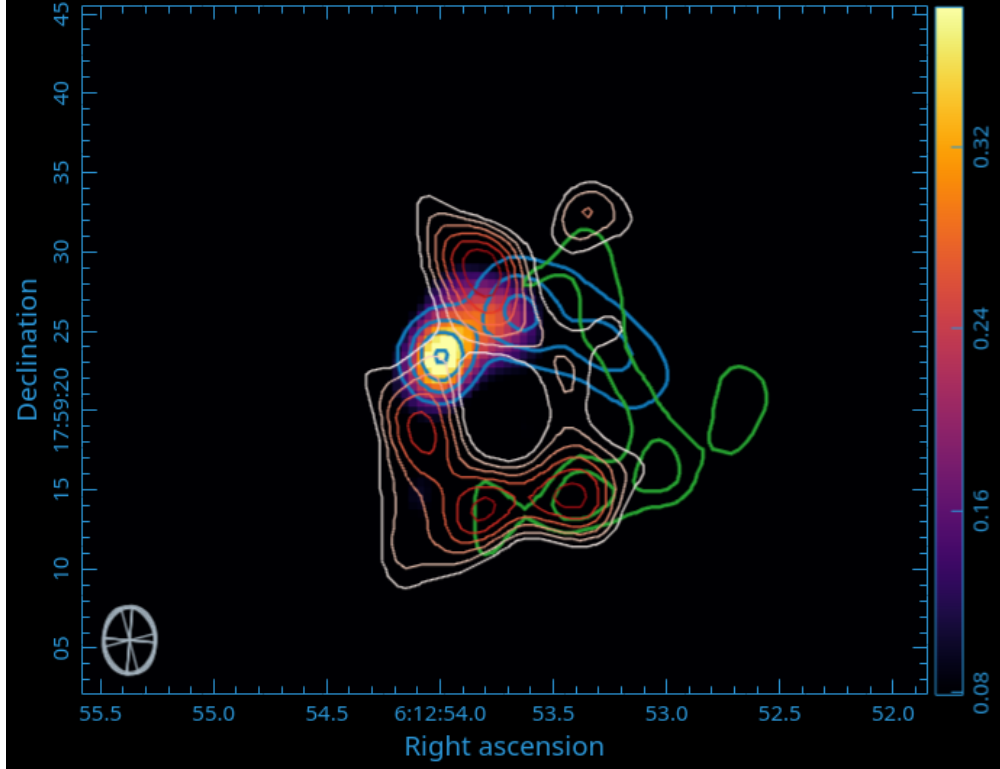
Optical depth of the SO line was determined using the ^{34}SO isotopologue; it was found to be 1.1 ± 0.2 .

VII. THE ORIGIN OF THE RING-SHAPED STRUCTURE

One of the interesting features of the S255IR region detected as a result of the observations is the ring-shaped structure visible in the lines of CN and some other molecules (see IV and Fig. 9) to the southeast of the SMA1–SMA3 region. It should be noted that no molecular emission was detected inside the ring, except for the weak emission of CO and its isotopologues ^{13}CO and $C^{18}O$. A structure similar to CN image in Fig. 9 was partially observed previously in CCH and $C^{34}S$ lines (see Figs. 4 and 6 in [9]). In addition, the contours of the $4_2 - 3_1$ methanol line in Fig. 9 roughly coincide with the CO and SiO images of the blue wing of the outflow from SMA2, presented in [9].

It is natural to assume that the ring is formed by the walls of the cavity, previously discovered by the observations of the light echo from the flare in NIRS3 ([16]). According to [16], this cavity is formed by the blue wing of the high-velocity outflow from NIRS3. However, it is possible that in addition to the NIRS3 outflow, the outflow from SMA2 (which at large distances may merge with the NIRS3 outflow) contributes to the formation of the cavity ([9]). Probably there is one more

Figure 9. Ring-shaped structure. The background represents the continuum emission at 1.3 mm. The white-red contours show the CN image in the 2-1 $J=3/2-1/2$ $F=5/2-3/2$ line at 226659.558 MHz; the contour levels are 1.34, 1.59, 1.85, 2.10, 2.36 and 2.61 Jy/beam. The green contours show the 5 – 4 HCS⁺ image at 213360.641 MHz; the contour levels are 0.62, 0.83 and 1.04 Jy/beam. The blue contours show the CH₃OH image in the 4₂ – 3₁E line at 218440.05 MHz; the contour levels are 4.31, 6.46, 8.61 and 10.76 Jy/beam.

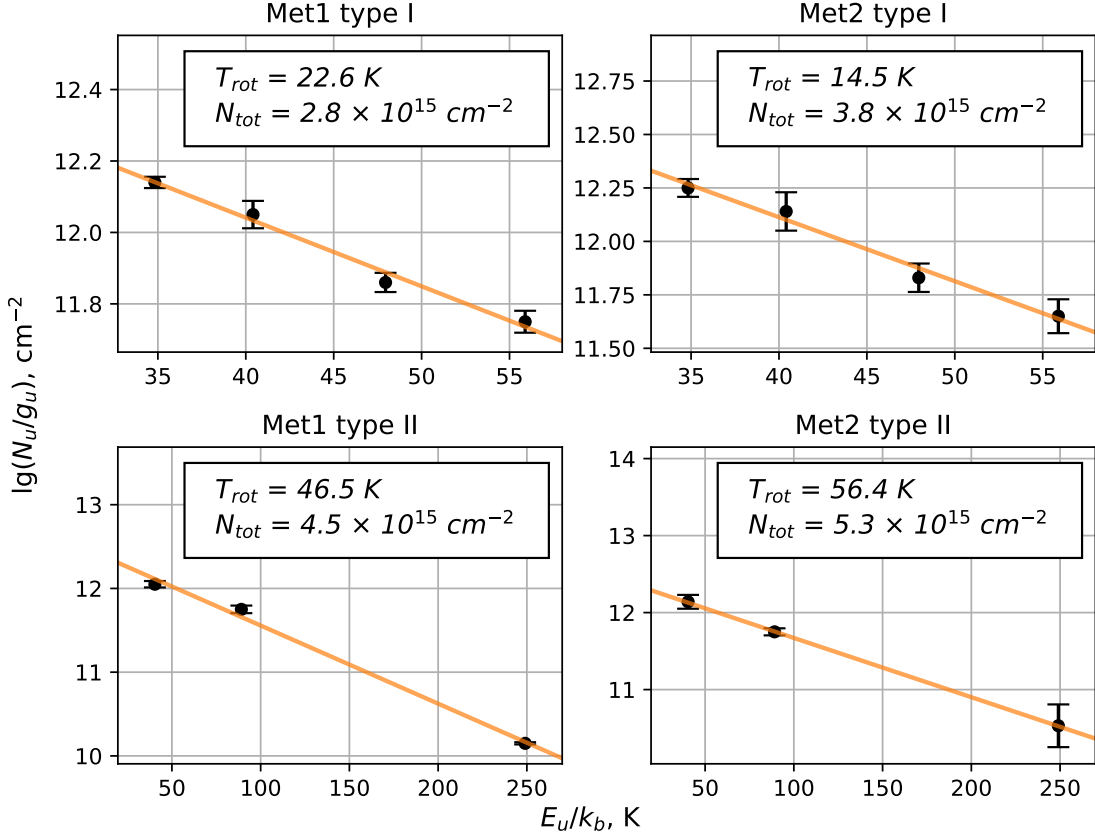


outflow in this region, accelerated by NIRS1 and propagating perpendicular to the line of sight ([8], [9]).

It is well known that many COMs are formed in the mantles of interstellar dust grains and enter the gas phase in large quantities during the evaporation or destruction of the mantles. Mantles evaporate when dust in the vicinity of protostars heats up to the temperature $\gtrsim 100$ K. The immediate vicinity of protostars with temperatures of the order of 100 K and higher, as well as with an increased content of complex molecules, are called hot cores. In hot cores, in particular, the content of oxygen-containing complex molecules (O-COMs) CH₃OH, HCOOH, CH₃CHO, CH₃OCHO, CH₃OCH₃ is greatly increased (e.g. Herbst & van Dishoeck [33]). It is therefore not surprising that in S255IR these molecules are observed toward the hot core SMA1.

In addition, the abundance of such molecules can increase in hot gas behind the shock fronts of high-velocity outflows. In these sources, the mantles of dust grains are destroyed by collisions with fast H₂ molecules in hot gas. In S255IR, shock waves should arise at the points where high-velocity outflows interact with the cavity walls. It is well known that in some such objects the abundance of methanol is increased by several orders of magnitude compared to its abundance in quiescent gas ([34], [35]), which leads to the appearance of strong emission in methanol lines. In addition, Arce et al. [27] reported the detection of HCOOH, CH₃OH, CH₃OCHO, and CH₃CH₂OH toward the blue wing of the high-velocity outflow from the low-mass YSO L1157, as well as measuring the abundance of these molecules relative to methanol. However, in S255IR, of the four molecules reported by Arce et al., we only detected methanol in the direction of the high-velocity outflows

Figure 10. Rotation diagrams of methanol toward Met1 (left column) and Met2 (right column). Top: RDs of type I. Bottom: RDs of type II.



associated with SMA1 and SMA2 (see Fig. 4,7). Hence, the question arises, whether the non-detection of these molecules is because their abundance relative to methanol in S255IR is lower than in L1157, or because our sensitivity is not sufficient to detect their emission?

To answer this question, we first estimated the temperatures, the number densities of H_2 molecules, and the column densities of methanol toward two brightness peaks of methanol, designated Met1 and Met2 (see Fig. 7). Estimates were made using RDs constructed from specifically selected CH_3OH lines. According to Kalenskii and Kurtz [36], an RD constructed using lines whose upper levels have the same rotational quantum number J , but different quantum numbers of the projection of the angular momentum of the molecule onto the symmetry axis K , allows one to determine the concentration of H_2 molecules rather than source temperature. Kalenskii and Kurtz [36] denoted such RDs as type I RDs. The rotational temperature obtained using type I RD can be very different from the ambient temperature, but is uniquely related to the number density of H_2 . If the rotation diagram is constructed using lines whose upper levels belong to the same K -ladder, i.e. have the same quantum number K , but different quantum numbers J , then the rotational temperature will be close to the gas temperature. Kalensky and Kurtz denoted such RDs as type II RDs. Figure 10 shows type I and II RDs toward Met1 and Met2. Type I RDs were constructed using the $5_K - 4_K$ lines. The obtained rotational temperatures ($\gtrsim 15$ K) correspond to H_2 number densities $\gtrsim 10^7 \text{ cm}^{-3}$; at such a high number density, the ratios of level populations are close to the values obtained as a result of collision thermalization, and the obtained methanol column densities ($N_{\text{CH}_3\text{OH}}$) are close to the real ones, according to Table 1 from [36].

Type II RDs are constructed from the methanol- E lines with the upper levels belonging to

a ladder with quantum number $K = -1$ (the backbone ladder). The T_{rot} and N_{CH_3OH} values yielded by such RD, at high concentrations of H_2 molecules, are practically equal to the kinetic temperature of the source and the column density of methanol. Therefore, we assume that in Met1 the gas temperature is 47 K and the column density of methanol is $4.5 \times 10^{15} \text{ cm}^{-2}$, and in Met2 these values are 56 K and $5.3 \times 10^{15} \text{ cm}^{-2}$.

Table III. Column densities of O-COMs in Met1 and Met2. Columns 3 and 5 show column densities of undetected here molecules HCOOH, CH_3OCHO , and CH_3CH_2OH , estimated based on methanol column densities in these objects. Columns 4 and 6 show the minimum values of column densities of these molecules required for them to be detectable with our sensitivity. The values are calculated assuming LTE at 50 K

Molecule	$N_{mol}/N_{CH_3OH}^1$	Met1		Met2	
		N_{mol}, cm^{-2}	$N_{mol}^{thr}, \text{cm}^{-2}$	N_{mol}, cm^{-2}	$N_{mol}^{thr}, \text{cm}^{-2}$
HCOOH	10^{-3}	4.5×10^{12}	5.2×10^{13}	5.3×10^{12}	5.0×10^{13}
CH_3OCHO	10^{-2}	4.5×10^{13}	1.3×10^{14}	5.3×10^{13}	1.2×10^{14}
CH_3CH_2OH	10^{-3}	4.5×10^{12}	4.9×10^{14}	5.3×10^{12}	4.3×10^{14}

¹—from Arce et al, 2008 [27]

Assuming that the abundances of HCOOH, CH_3OCHO , and CH_3CH_2OH relative to methanol are equal to those obtained by Arce et al. [27], we calculated column densities of these molecules in Met1 and Met2. The results are presented in Table III (third and fifth columns). Assuming that the rotational temperatures of HCOOH, CH_3OCHO , and CH_3CH_2OH coincide with the rotational temperatures of methanol, we calculated, assuming LTE, the column densities of these molecules that would make them detectable with our sensitivity. We denote these values N_{mol}^{thr} ; they are given in columns 4 and 6 of Table III. Comparison of the values in the third column with those in the fourth column and in the fifth column with those in the sixth column shows that at our sensitivity we would not detect the emission of these complex oxygen-containing molecules toward the wings of the high-velocity outflows in S255IR. In subsequent work, we expect to decrease the detection thresholds for complex molecules using spectral line stacking and either detect O-COMs in Met1 and Met2 or show that the O-COM to methanol abundance ratios in S255IR are lower than in L1157.

VIII. SUMMARY AND CONCLUSION

Using the SMA antenna array we performed interferometric observations of the star-forming region S255IR in the 210–250 GHz frequency range. As a result, emission of 53 molecules was detected, including COMs CH_3OCHO , CH_3OCH_3 , CH_3CH_2OH , and numerous others. Maps of the region were built for a large number of molecular lines, and spectra of the SMA1 and SMA2 cores were obtained.

Most of the detected molecules can be roughly divided into two groups. Molecules of the first group emit exclusively toward the hot core SMA1, while molecules of the second group, in addition to SMA1, emit toward a ring-shaped structure west of SMA1. This structure appears to be associated with the walls of a cavity formed by high-velocity outflows from the YSOs in molecular cores SMA1, SMA2, and possibly SMA3. Brightness peaks of methanol, clearly visible toward the ring-shaped structure, may be associated with shock waves resulting from the interaction between the outflows and the cavity walls.

We constructed rotation diagrams for 13 COMs detected in SMA1. Rotational temperatures for most of these molecules fall in the range of 100–200 K. Higher rotational temperatures were found for HCOOH ($T_{rot} = 359$ K) and CH_3CN ($T_{rot} = 279$ K). CH_3CH_2CN has a lower rotational temperature

($T_{rot} = 36$ K). Methyl acetylene, which is considered a good "thermometer" for interstellar gas, has a negative rotational temperature, which likely indicates absorption of the K=0 and 1 emission in a cold shell.

Optical depths of the lines of several molecules in the SMA1 and SMA2 cores were estimated. In SMA1, the optical depth in the $5_{-1} - 4_{-1}E$ methanol line proved to be 23.8 ± 1.5 . Since numerous studies show that the abundance of COMs such as CH_3CHO , CH_3OCHO , or $\text{C}_2\text{H}_5\text{OH}$ in the hot gas is 30 or more times lower than the abundance of methanol, we assume that the emission of these COMs is optically thin and hence the optical depths do not affect the rotation diagrams. The optical depth in the $3_{1,2} - 2_{1,2}$ formaldehyde line was found to be 12.3 ± 1.0 , in the $5 - 4$ CS line, 4.3 ± 0.5 , in the $N, J = 5, 6 - 4, 5$ SO line, 2.70 ± 0.5 , and in the $18 - 17$ and $20 - 19$ OCS lines, 2.2 ± 1.2 and 1.4 ± 0.3 , respectively.

In SMA2, the optical depth of the $5 - 4$ CS line was found to be 4.8 ± 1.6 , and the $N, J = 5, 6 - 4, 5$ SO line, 1.1 ± 0.2 .

Using methanol lines, gas temperature and density were estimated toward two objects seen as methanol brightness peaks Met1 and Met2. The temperature and density were found to be on the order of 50-60 K and $10^7 - 10^8 \text{ cm}^{-3}$. Methanol column density in Met1 was found to be $5.4 \times 10^{15} \text{ cm}^{-2}$, and in Met2 — $4.0 \times 10^{15} \text{ cm}^{-2}$. Column densities of other COMs in the ring-shaped structure will be determined in future studies with increased sensitivity using spectral line stacking.

ACKNOWLEDGMENTS

The authors thanks prof. I. I. Zinchenko, S. V. Salii and P. A. Tanatova for useful discussions and to the anonymous referee for helpful comments. They are grateful for the support from the SMA operators during the observations.

The Submillimeter Array is a joint project between the Smithsonian Astrophysical Observatory and the Academia Sinica Institute of Astronomy and Astrophysics and is funded by the Smithsonian Institution and the Academia Sinica.

We recognize that Maunakea is a culturally important site for the indigenous Hawaiian people; we are privileged to study the cosmos from its summit.

CONFLICT OF INTEREST

The authors declare no conflict of interest.

[1] R. Burns, T. Handa, T. Nagayama, K. Sunada, and T. Omodaka, *Monthly Notices of the Royal Astronomical Society* **460**, 283 (2016).

[2] R. L. Snell and J. Bally, *Astrophys. J.* **303**, 683 (1986).

[3] D. K. Ojha, M. R. Samal, A. K. Pandey, B. C. Bhatt, S. K. Ghosh, S. Sharma, M. Tamura, V. Mohan, and I. Zinchenko, *Astrophysical Journal* **738**, 156 (2011).

[4] Y. Wang, H. Beuther, A. Bik, T. Vasyunina, Z. Jiang, E. Puga, H. Linz, J. A. Rodón, T. Henning, and M. Tamura, *Astronomy & Astrophysics* **527**, A32 (2011), ISSN 1432-0746, URL <http://dx.doi.org/10.1051/0004-6361/201015543>.

[5] V. Minier, R. S. Booth, and J. E. Conway, *Astronomy & Astrophysics* **362**, 1093–1108 (2000).

[6] C. Goddi, L. Moscadelli, A. Sanna, R. Cesaroni, and V. Minier, *Astronomy & Astrophysics* **461**, 1027 (2007).

[7] V. Minier, M. G. Burton, T. Hill, M. R. Pestalozzi, C. R. Purcell, G. Garay, A. J. Walsh, and S. Longmore, *Astronomy & Astrophysics* **429**, 945–960 (2005), ISSN 1432-0746, URL <http://dx.doi.org/10.1051/0004-6361:20041137>.

[8] J. P. Simpson, M. G. Burton, S. W. J. Colgan, A. S. Cotera, E. F. Erickson, D. C. Hines, and B. A. Whitney, *The Astrophysical Journal* **700**, 1488–1501 (2009), ISSN 1538-4357, URL <http://dx.doi.org/10.1088/0004-637X/700/2/1488>.

[9] I. I. Zinchenko, S.-Y. Liu, Y.-N. Su, K.-S. Wang, and Y. Wang, *The Astrophysical Journal* **889**, 43 (2020), ISSN 1538-4357, URL <http://dx.doi.org/10.3847/1538-4357/ab5c18>.

[10] I. Zinchenko, S.-Y. Liu, Y.-N. Su, S. Kurtz, D. K. Ojha, M. R. Samal, and S. K. Ghosh, *The Astrophysical Journal* **755**, 177 (2012), ISSN 1538-4357, URL <http://dx.doi.org/10.1088/0004-637X/755/2/177>.

[11] I. Zinchenko, S.-Y. Liu, Y.-N. Su, S. V. Salii, A. M. Sobolev, P. Zemlyanukha, H. Beuther, D. K. Ojha, M. R. Samal, and Y. Wang, *The Astrophysical Journal* **810**, 10 (2015), ISSN 1538-4357, URL <http://dx.doi.org/10.1088/0004-637X/810/1/10>.

[12] P. A. Boley, H. Linz, R. van Boekel, T. Henning, M. Feldt, L. Kaper, C. Leinert, A. Müller, I. Pascucci, M. Roberto, *et al.*, *Astronomy & Astrophysics* **558**, A24 (2013), ISSN 1432-0746, URL <http://dx.doi.org/10.1051/0004-6361/201321539>.

[13] Y. Wang, H. Beuther, A. Bik, T. Vasyunina, Z. Jiang, E. Puga, H. Linz, J. Rodon, T. Henning, and M. Tamura, *Astronomy and Astrophysics* **527** (2010).

[14] K. Fujisawa, Y. Yonekura, K. Sugiyama, H. Horiuchi, T. Hayashi, K. Hachisuka, N. Matsumoto, and K. Niiuma, *The Astronomer's Telegram* No. 8286 (2015), URL <https://www.astronomerstelegram.org/?read=8286>.

[15] B. Stecklum, A. C. o Garatti, M. C. Cardenas, J. Greiner, T. Kruehler, S. Klose, and J. Eisloeffel, *The Astronomer's Telegram*, No. 8732 (2016), URL <https://www.astronomerstelegram.org/?read=8732>.

[16] A. Caratti o Garatti, B. Stecklum, R. Garcia Lopez, J. Eislöffel, T. P. Ray, A. Sanna, R. Cesaroni, C. Walmsley, R. D. Oudmaijer, W. J. de Wit, *et al.*, *Nature Physics* **13**, 276–279 (2017), ISSN 1745-2481, URL <http://dx.doi.org/10.1038/nphys3942>.

[17] M. Uchiyama, T. Yamashita, K. Sugiyama, T. Nakaoka, M. Kawabata, R. Itoh, M. Yamanaka, H. Akitaya, K. Kawabata, Y. Yonekura, *et al.*, *Publications of the Astronomical Society of Japan* **72** (2019), ISSN 2053-051X, URL <http://dx.doi.org/10.1093/pasj/psz122>.

[18] I. Zinchenko, S. Liu, D. Ojha, Y. Su, and P. Zemlyanukha, in *Modern astronomy: from the Early Universe to exoplanets and black holes* (Special Astrophysical Observatory of the Russian Academy of Sciences, 2024), p. 604–610, URL <http://dx.doi.org/10.26119/VAK2024.096>.

[19] S.-Y. Liu, Y.-N. Su, I. Zinchenko, K.-S. Wang, D. M.-A. Meyer, Y. Wang, and I.-T. Hsieh, *The Astrophysical Journal* **904**, 181 (2020), ISSN 1538-4357, URL <http://dx.doi.org/10.3847/1538-4357/abc0ec>.

[20] R. Fedriani, A. Caratti o Garatti, R. Cesaroni, J. C. Tan, B. Stecklum, L. Moscadelli, M. Koutoulaki, G. Cosentino, and M. Whittle, *Astronomy & Astrophysics* **676**, A107 (2023), ISSN 1432-0746, URL <http://dx.doi.org/10.1051/0004-6361/202346736>.

[21] S.-Y. Liu, Y.-N. Su, I. Zinchenko, K.-S. Wang, and Y. Wang, *The Astrophysical Journal Letters* **863**, L12 (2018), ISSN 2041-8213, URL <http://dx.doi.org/10.3847/2041-8213/aad63a>.

- [22] B. J. Hazelton, D. C. Jacobs, J. C. Pober, and A. P. Beardsley, The Journal of Open Source Software **2**, 140 (2017).
- [23] G. Keating, B. Hazelton, M. Kolopanis, S. Murray, A. Beardsley, D. Jacobs, N. Kern, A. Lanman, P. La Plante, J. Pober, *et al.*, The Journal of Open Source Software **10**, 7482 (2025).
- [24] A. Comrie, K.-S. Wang, Y.-H. Hwang, A. Moraghan, P. Harris, A. Pińska, C. Raul-Omar, K.-C. Hou, C.-C. Chiang, T.-H. Chang, *et al.*, *CARTA: The Cube Analysis and Rendering Tool for Astronomy* (2018), URL <https://doi.org/10.5281/zenodo.3377984>.
- [25] X. Chen, Z.-Y. Ren, D.-L. Li, T. Liu, K. Wang, Z.-Q. Shen, S. P. Ellingsen, A. M. Sobolev, Y. Mei, J.-J. Li, *et al.*, The Astrophysical Journal Letters **923**, L20 (2021).
- [26] S. N. Milam, C. Savage, M. A. Brewster, L. M. Ziurys, and S. Wyckoff, *Astrophys. J.* **634**, 1126 (2005).
- [27] H. G. Arce, J. Santiago-García, J. K. Jørgensen, M. Tafalla, and R. Bachiller, The Astrophysical Journal **681**, L21–L24 (2008), ISSN 1538-4357, URL <http://dx.doi.org/10.1086/590110>.
- [28] S. V. Kalenskii and L. E. B. Johansson, *Astronomy Reports* **54**, 1084 (2010).
- [29] A. Belloche, H. S. P. Muller, K. M. Menten, P. Schilke, and C. Comito, *Astronomy & Astrophysics* **559**, 47 (2013).
- [30] S. V. Kalenskii, R. I. Kaiser, P. Bergman, A. O. H. Olofsson, K. D. Degtyarev, and P. Golysheva, The Astrophysical Journal **932** (2022), ISSN 1538-4357.
- [31] Y. Chen, M. L. van Gelder, P. Nazari, C. L. Brogan, E. F. van Dishoeck, H. Linnartz, J. K. Jørgensen, T. R. Hunter, O. H. Wilkins, G. A. Blake, *et al.*, *Astronomy & Astrophysics* **678**, A137 (2023).
- [32] T. L. Wilson and R. T. Rood, *Annual Review of Astronomy and Astrophysics* **32**, 191 (1994).
- [33] E. Herbst and E. F. van Dishoeck, *Annual Review of Astronomy and Astrophysics* **47**, 427 (2009).
- [34] R. Bachiller, S. Liechti, C. M. Walmsley, and F. Colomer, *Astronomy and Astrophysics* **295**, L51–L54 (1995), URL <https://articles.adsabs.harvard.edu/pdf/1995A%26A...295L..51B>.
- [35] R. Bachiller and M. Pérez Gutiérrez, *Astronomy and Astrophysics* **487**, L93–L96 (1997), URL <https://iopscience.iop.org/article/10.1086/310877>.
- [36] S. V. Kalenskii and S. Kurtz, *Astronomy Reports* **60**, 702 (2016).

APPENDIX

Table IV: Spectral lines for which maps were constructed and which were used to build rotation diagrams. Comments: map — a map was constructed for this line; rd — the line was used for the rotation diagram.

Molecule	Frequency (MHz)	Transition	Low level energy (cm ⁻¹)	Comments
¹³ CO	220398.684	2 – 1	3.6759	map
C ¹⁷ O	224714.389	2 – 1	3.7479	map
C ¹⁸ O	219560.358	2 – 1	3.6619	map
C ³⁴ S	241016.089	5 – 4	16.0796	map
CH ₂ CO	220177.416	11 _{1,11} – 10 _{1,10}	45.8108	rd
CH ₂ CO	222228.587	11 _{2,10} – 10 _{2,9}	73.4814	rd
CH ₂ CO	222314.457	11 _{2,9} – 10 _{2,8}	73.4878	rd
CH ₂ CO	224327.250	11 _{1,10} – 10 _{1,9}	46.4891	map, rd
CH ₂ CO	240185.612	12 _{1,12} – 11 _{1,11}	53.1551	rd
CH ₂ CO	242309.307	12 _{4,9} – 11 _{4,8}	191.2698	rd
+CH ₂ CO	242309.308	12 _{4,8} – 11 _{4,7}	191.2698	rd
CH ₂ CO	242375.380	12 _{0,12} – 11 _{0,11}	44.4798	rd
CH ₂ CO	242398.458	12 _{3,10} – 11 _{3,9}	126.6753	rd
+CH ₂ CO	242398.956	12 _{3,9} – 11 _{3,8}	126.6753	rd
CH ₂ CO	242424.606	12 _{2,11} – 11 _{2,10}	80.8941	rd
CH ₂ CO	244712.079	12 _{1,11} – 11 _{1,10}	53.9858	rd
CH ₃ CCH	222128.812	13 ₃ – 12 ₃	89.5037	rd
CH ₃ CCH	222150.008	13 ₂ – 12 ₂	64.4833	rd
CH ₃ CCH	222162.729	13 ₁ – 12 ₁	49.4710	rd
CH ₃ CCH	222166.971	13 ₀ – 12 ₀	44.4669	map, rd
CH ₃ CCH	239211.212	14 ₃ – 13 ₃	96.9131	rd
CH ₃ CCH	239234.032	14 ₂ – 13 ₂	71.8934	rd
CH ₃ CCH	239247.727	14 ₁ – 13 ₁	56.8816	rd
CH ₃ CCH	239252.294	14 ₀ – 13 ₀	51.8776	map, rd
CH ₃ CH ₂ CN	215039.727	24 _{9,*} – 23 _{9,*}	145.0122	rd
+CH ₃ CH ₂ CN	215041.902	24 _{10,*} – 23 _{10,*}	159.6548	rd
CH ₃ CH ₂ CN	215109.050	24 _{7,*} – 23 _{7,*}	120.3350	rd
CH ₃ CH ₂ CN	215119.210	25 _{0,25} – 24 _{0,24}	87.2402	rd
CH ₃ CH ₂ CN	215965.588	25 _{1,25} – 24 _{0,24}	87.2402	rd
CH ₃ CH ₂ CN	215941.073	6 _{4,3} – 5 _{3,2}	11.4397	rd
CH ₃ CH ₂ CN	222918.177	25 _{1,24} – 24 _{1,23}	91.4821	rd
CH ₃ CH ₂ CN	223553.585	26 _{0,26} – 25 _{0,25}	94.4158	rd
CH ₃ CH ₂ CN	225236.118	25 _{4,21} – 24 _{4,20}	102.1946	map, rd
CH ₃ CH ₂ CN	225317.146	23 _{2,22} – 22 _{1,21}	77.4544	rd
CH ₃ CH ₂ CN	227780.978	25 _{3,22} – 24 _{3,21}	97.2481	rd
CH ₃ CH ₂ CN	231854.217	27 _{1,27} – 26 _{1,26}	101.8954	rd
CH ₃ CH ₂ CN	235051.950	13 _{3,10} – 12 _{2,11}	26.3395	rd
CH ₃ CH ₂ CN	241922.546	27 _{10,*} – 26 _{10,*}	182.0705	rd
CH ₃ CH ₂ CN	245023.654	14 _{3,11} – 13 _{2,12}	30.2053	rd
CH ₃ CH ₂ CN	248617.257	16 _{3,14} – 15 _{2,13}	39.3323	rd
g-CH ₃ CH ₂ OH	225109.881	13 _{6,*} – 12 _{6,*} ν _t = 1 – 1	118.6281	rd
g-CH ₃ CH ₂ OH	225170.614	13 _{7,*} – 12 _{7,*} ν _t = 0 – 0	126.1147	rd
g-CH ₃ CH ₂ OH	225248.812	13 _{6,*} – 12 _{6,*} ν _t = 0 – 0	115.0929	rd
g-CH ₃ CH ₂ OH	225399.733	13 _{5,9} – 12 _{5,8} ν _t = 0 – 0	105.7788	rd
g-CH ₃ CH ₂ OH	225404.089	13 _{5,8} – 12 _{5,7} ν _t = 0 – 0	105.7789	rd
g-CH ₃ CH ₂ OH	227760.743	3 _{2,2} – 2 _{1,2} ν _t = 1 – 0	42.0627	rd

Molecule	Frequency (MHz)	Transition	Low level energy (cm ⁻¹)	Comments
g-CH ₃ CH ₂ OH	228029.050	13 _{3,10} – 12 _{3,9} ν_t = 0 – 0	92.4075	rd
g-CH ₃ CH ₂ OH	230793.506	6 _{5,1} – 5 _{4,1} ν_t = 0 – 1	65.1423	rd
+g-CH ₃ CH ₂ OH	230793.506	6 _{5,2} – 5 _{4,2} ν_t = 0 – 1	65.1423	rd
+ AlF	230793.905	7 – 6	23.098	
g-CH ₃ CH ₂ OH	231668.733	14 _{1,14} – 13 _{1,13} ν_t = 0 – 0	90.9002	rd
g-CH ₃ CH ₂ OH	232491.366	14 _{0,14} – 13 _{0,13} ν_t = 0 – 0	90.7911	rd
g-CH ₃ CH ₂ OH	232596.554	14 _{1,14} – 13 _{0,13} ν_t = 1 – 1	94.0893	rd
g-CH ₃ CH ₂ OH	238568.317	6 _{1,5} – 5 _{0,5} ν_t = 1 – 0	48.1500	rd
g-CH ₃ CH ₂ OH	239478.079	14 _{2,13} – 13 _{2,12} ν_t = 0 – 0	95.1822	rd
g-CH ₃ CH ₂ OH	239551.366	14 _{2,13} – 13 _{2,12} ν_t = 1 – 1	98.4279	rd
g-CH ₃ CH ₂ OH	242349.842	14 _{7,*} – 13 _{7,*} ν_t = 1 – 1	137.2373	rd
g-CH ₃ CH ₂ OH	242685.010	14 _{5,10} – 13 _{5,9} ν_t = 1 – 1	116.7465	rd
g-CH ₃ CH ₂ OH	242770.099	14 _{3,12} – 13 _{3,11} ν_t = 1 – 1	103.0917	rd
g-CH ₃ CH ₂ OH	243120.317	14 _{4,11} – 13 _{4,10}	105.7049	map, rd
g-CH ₃ CH ₂ OH	244633.950	14 _{1,13} – 13 _{1,12} ν_t = 1 – 1	97.3154	rd
g-CH ₃ CH ₂ OH	245327.139	14 _{3,11} – 13 _{3,10} ν_t = 1 – 1	103.2617	rd
g-CH ₃ CH ₂ OH	246414.762	14 _{3,11} – 13 _{3,10} ν_t = 0 – 0	100.0137	rd
g-CH ₃ CH ₂ OH	248178.548	15 _{1,15} – 14 _{1,14} ν_t = 1 – 1	101.8479	rd
g-CH ₃ CH ₂ OH	248463.614	14 _{2,12} – 13 _{2,11} ν_t = 0 – 0	96.3457	rd
g-CH ₃ CH ₂ OH	248577.119	15 _{0,15} – 14 _{0,14} ν_t = 0 – 0	98.5462	rd
t-CH ₃ CH ₂ OH	218554.382	21 _{5,16} – 21 _{4,17}	149.7973	rd
t-CH ₃ CH ₂ OH	218654.008	7 _{2,5} – 6 _{1,6}	12.6749	rd
t-CH ₃ CH ₂ OH	225229.253	17 _{2,15} – 16 _{3,14}	87.3973	rd
t-CH ₃ CH ₂ OH	229491.13	17 _{5,12} – 17 _{4,13}	103.6309	rd
t-CH ₃ CH ₂ OH	230991.377	14 _{0,14} – 13 _{1,13}	51.7390	rd
t-CH ₃ CH ₂ OH	231737.593	19 _{5,15} – 19 _{4,16}	125.2481	rd
t-CH ₃ CH ₂ OH	231790.000	22 _{5,18} – 22 _{4,19}	162.2344	rd
t-CH ₃ CH ₂ OH	232034.630	18 _{5,14} – 18 _{4,15}	114.0935	rd
t-CH ₃ CH ₂ OH	232075.864	15 _{5,10} – 15 _{4,11}	84.2068	rd
t-CH ₃ CH ₂ OH	232318.469	23 _{5,19} – 23 _{4,20}	175.7316	rd
t-CH ₃ CH ₂ OH	232928.552	14 _{5,9} – 14 _{4,10}	75.3953	rd
t-CH ₃ CH ₂ OH	233571.082	13 _{5,8} – 13 _{4,9}	67.1801	rd
t-CH ₃ CH ₂ OH	233951.264	13 _{5,9} – 13 _{4,10}	67.1670	rd
t-CH ₃ CH ₂ OH	234051.178	12 _{5,7} – 12 _{4,8}	59.5587	rd
t-CH ₃ CH ₂ OH	234255.161	12 _{5,8} – 12 _{4,9}	59.5518	map, rd
t-CH ₃ CH ₂ OH	234406.456	11 _{5,6} – 11 _{4,7}	52.5292	rd
t-CH ₃ CH ₂ OH	234666.157	10 _{5,5} – 10 _{4,6}	46.0900	rd
t-CH ₃ CH ₂ OH	234758.820	6 _{3,4} – 5 _{2,3}	12.2822	map, rd
t-CH ₃ CH ₂ OH	234852.866	9 _{5,4} – 9 _{4,5}	40.2396	rd
t-CH ₃ CH ₂ OH	234873.877	9 _{5,5} – 9 _{4,6}	40.2389	rd
t-CH ₃ CH ₂ OH	234984.050	8 _{5,3} – 8 _{4,4}	34.9769	rd
t-CH ₃ CH ₂ OH	234992.183	8 _{5,4} – 8 _{4,5}	34.9766	rd
t-CH ₃ CH ₂ OH	235073.313	7 _{5,2} – 7 _{4,3}	30.3011	rd
t-CH ₃ CH ₂ OH	235131.372	6 _{5,1} – 6 _{4,2}	26.2113	rd
t-CH ₃ CH ₂ OH	236146.424	15 _{1,14} – 14 _{2,13}	64.3344	rd
t-CH ₃ CH ₂ OH	238667.995	27 _{5,23} – 27 _{4,24}	235.4995	rd
t-CH ₃ CH ₂ OH	243556.853	8 _{2,6} – 7 _{1,7}	16.5989	rd
CH ₃ CHO	216581.924	11 _{1,10} – 10 _{1,9} <i>E</i>	37.8632	rd
CH ₃ CHO	223650.097	12 _{-1,12} – 11 _{-1,11} <i>E</i>	42.7701	rd
CH ₃ CHO	223660.610	12 _{1,12} – 11 _{1,11} <i>A</i> ⁺⁺	42.7701	rd
CH ₃ CHO	224656.971	12 _{3,9} – 12 _{2,10} <i>A</i> ⁻⁺	56.8839	rd
CH ₃ CHO	226487.236	13 _{0,13} – 12 _{-1,12} <i>E</i>	50.2302	rd
CH ₃ CHO	226551.622	12 _{0,12} – 11 _{0,11} <i>E</i>	42.0628	map,rd

Molecule	Frequency (MHz)	Transition	Low level energy (cm ⁻¹)	Comments
CH ₃ CHO	226592.725	12 _{0,12} – 11 _{0,11} A ⁺⁺	42.0013	map,rd
CH ₃ CHO	227258.988	12 _{0,12} – 11 _{0,11} E $\nu_t = 1$	184.0719	rd
CH ₃ CHO	229432.106	11 _{-1,11} – 10 _{0,10} E	35.1170	rd
CH ₃ CHO	229775.029	11 _{1,11} – 10 _{0,10} A ⁺⁺	35.0542	rd
CH ₃ CHO	230301.924	12 _{2,11} – 11 _{2,10} A ⁻⁻	48.6454	rd
CH ₃ CHO	230315.788	12 _{-2,11} – 11 _{-2,10} E	48.6543	rd
CH ₃ CHO	230395.155	12 _{2,11} – 11 _{2,10} A ⁻⁻ $\nu_t = 1$	191.378	rd
CH ₃ CHO	231363.289	12 _{-5,7} – 11 _{-5,6} E	81.6239	rd
CH ₃ CHO	231369.834	12 _{5,8} – 11 _{5,7} E	81.6023	rd
CH ₃ CHO	231456.738	12 _{4,9} – 11 _{4,8} A ⁻⁻	67.5887	rd
CH ₃ CHO	231467.499	12 _{4,8} – 11 _{4,7} A ⁺⁺	67.5891	rd
CH ₃ CHO	231506.297	12 _{-4,9} – 11 _{-4,8} E	67.5167	rd
CH ₃ CHO	231595.269	12 _{3,10} – 11 _{3,9} A ⁺⁺	56.6212	rd
CH ₃ CHO	231748.722	12 _{-3,10} – 11 _{-3,9} E	56.5679	rd
CH ₃ CHO	231847.575	12 _{3,9} – 11 _{3,8} E	56.6340	rd
CH ₃ CHO	234795.450	12 _{2,10} – 11 _{2,9} E	49.0668	rd
CH ₃ CHO	234825.872	12 _{2,10} – 11 _{2,9} A ⁺⁺	49.0510	map,rd
CH ₃ CHO	234842.78	6 _{3,3} – 6 _{2,4} A	19.8344	rd
CH ₃ CHO	235217.832	12 _{1,11} – 11 _{1,10} A ⁻⁻ $\nu_t = 1$	188.3389	rd
CH ₃ CHO	235996.212	12 _{1,11} – 11 _{1,10} E	45.0876	map
+ ¹³ CH ₃ OH	235997.230	5 ₃ – 4 ₃	50.531	
CH ₃ CHO	242106.023	13 _{-1,13} – 12 _{-1,12} E	50.2302	rd
CH ₃ CHO	242118.143	13 _{1,13} – 12 _{1,12} A ⁺⁺	50.1792	rd
CH ₃ CHO	243178.657	13 _{1,13} – 12 _{1,12} E $\nu_t = 1$	192.2766	rd
CH ₃ CHO	243975.379	14 _{3,12} – 14 _{2,13} A ⁺⁻	73.5938	rd
CH ₃ CHO	244789.251	13 _{0,13} – 12 _{0,12} E	49.6197	map,rd
CH ₃ CHO	244832.176	13 _{0,13} – 12 _{0,12} A	49.5596	map,rd
CH ₃ CN	220475.822	12 ₈ – 11 ₈	357.9389	rd
CH ₃ CN	220539.335	12 ₇ – 11 ₇	283.6085	rd
CH ₃ CN	220641.089	12 ₅ – 11 ₅	164.5919	rd
CH ₃ CN	220679.287	12 ₄ – 11 ₄	119.9327	map, rd
CH ₃ CN	220709.017	12 ₃ – 11 ₃	85.1873	map, rd
CH ₃ CN	220730.261	12 ₂ – 11 ₂	60.3634	map, rd
CH ₃ CN	220743.011	12 ₁ – 11 ₁	45.4669	map
CH ₃ CN	220747.262	12 ₀ – 11 ₀	40.5010	map
CH ₃ CN	238843.942	13 ₈ – 12 ₈	365.2932	rd
CH ₃ CN	238912.727	13 ₇ – 12 ₇	290.9649	rd
CH ₃ CN	238972.398	13 ₆ – 12 ₆	226.5128	rd
CH ₃ CN	239022.929	13 ₅ – 12 ₅	171.9517	rd
CH ₃ CN	239064.299	13 ₄ – 12 ₄	127.2938	map, rd
CH ₃ CN	239096.497	13 ₃ – 12 ₃	92.5493	map, rd
CH ₃ CN	239119.505	13 ₂ – 12 ₂	67.7262	map, rd
CH ₃ CN	239137.917	13 ₀ – 12 ₀	47.8643	map
CH ₃ OCH ₃	222433.653	4 _{3,1} – 3 _{2,2} EE	7.7030	rd
+CH ₃ OCH ₃	222433.931	4 _{3,1} – 3 _{2,2} AA	7.7028	rd
+CH ₃ OCH ₃	222435.123	4 _{3,1} – 3 _{2,2} EA	7.7032	rd
CH ₃ OCH ₃	223200.063	8 _{2,7} – 7 _{1,6} EA	19.1811	rd
+CH ₃ OCH ₃	223200.072	8 _{2,7} – 7 _{1,6} AE	19.1811	rd
+CH ₃ OCH ₃	223202.243	8 _{2,7} – 7 _{1,6} EE	19.1809	rd
+CH ₃ OCH ₃	223204.418	8 _{2,7} – 7 _{1,6} AA	19.1806	rd
CH ₃ OCH ₃	223406.886	26 _{2,24} – 26 _{1,25} AE + EA	222.1807	rd
+CH ₃ OCH ₃	223409.478	26 _{2,24} – 26 _{1,25} EE	222.1807	rd
+CH ₃ OCH ₃	223412.069	26 _{2,24} – 26 _{1,25} AA	222.1806	rd

Molecule	Frequency (MHz)	Transition	Low level energy (cm ⁻¹)	Comments
CH ₃ OCH ₃	225598.770	12 _{1,12} – 11 _{0,11} EA + AE	40.9815	rd
+CH ₃ OCH ₃	225599.120	12 _{1,12} – 11 _{0,11} EE	40.9813	rd
+CH ₃ OCH ₃	225599.469	12 _{1,12} – 11 _{0,11} AA	40.9810	rd
CH ₃ OCH ₃	226346.124	14 _{1,13} – 13 _{2,12} AA	61.1644	rd
+CH ₃ OCH ₃	226346.948	14 _{1,13} – 13 _{2,12} EE	61.1646	rd
+CH ₃ OCH ₃	226347.772	14 _{1,13} – 13 _{2,12} AE + EA	61.1647	rd
CH ₃ OCH ₃	230140.140	25 _{4,22} – 25 _{3,23} AE + EA	214.1889	rd
+CH ₃ OCH ₃	230141.425	25 _{4,22} – 25 _{3,23} EE	214.1889	rd
+CH ₃ OCH ₃	230142.710	25 _{4,22} – 25 _{3,23} AA	214.1889	rd
CH ₃ OCH ₃	230232.166	17 _{2,15} – 16 _{3,14} AA	94.9454	rd
+CH ₃ OCH ₃	230233.749	17 _{2,15} – 16 _{3,14} EE	94.9454	rd
+CH ₃ OCH ₃	230235.333	17 _{2,15} – 16 _{3,14} AE + EA	94.9455	rd
CH ₃ OCH ₃	231987.779	13 _{0,13} – 12 _{1,12} AA	48.5062	rd
+CH ₃ OCH ₃	231987.856	13 _{0,13} – 12 _{1,12} EE	48.5064	rd
+CH ₃ OCH ₃	231987.933	13 _{0,13} – 12 _{1,12} AE + EA	48.5067	rd
CH ₃ OCH ₃	237618.821	9 _{2,8} – 8 _{1,7} EA	24.3654	rd
+CH ₃ OCH ₃	237618.826	9 _{2,8} – 8 _{1,7} AE	24.3654	rd
+CH ₃ OCH ₃	237620.888	9 _{2,8} – 8 _{1,7} EE	24.3651	rd
+CH ₃ OCH ₃	237622.953	9 _{2,8} – 8 _{1,7} AA	24.3649	rd
CH ₃ OCH ₃	240978.250	5 _{3,3} – 4 _{2,2} EA	10.2472	map
+CH ₃ OCH ₃	240982.770	5 _{3,3} – 4 _{2,2} AE	10.2472	map, rd
+CH ₃ OCH ₃	240985.067	5 _{3,3} – 4 _{2,2} EE	10.2472	map, rd
+CH ₃ OCH ₃	240989.973	5 _{3,3} – 4 _{2,2} AA	10.2468	rd
CH ₃ OCH ₃	241528.320	5 _{3,2} – 4 _{2,3} EA	10.2298	rd
+CH ₃ OCH ₃	241528.710	5 _{3,2} – 4 _{2,3} EE	10.2296	rd
+CH ₃ OCH ₃	241531.009	5 _{3,2} – 4 _{2,3} AA	10.2294	rd
CH ₃ OCH ₃	241946.2015	13 _{1,13} – 12 _{0,12} EA	48.3184	map, rd
+CH ₃ OCH ₃	241946.2018	13 _{1,13} – 12 _{0,12} AE	48.3184	map, rd
+CH ₃ OCH ₃	241946.4965	13 _{1,13} – 12 _{0,12} EE	48.3184	map, rd
+CH ₃ OCH ₃	241946.7913	13 _{1,13} – 12 _{0,12} AA	48.3184	map, rd
CH ₃ OCH ₃	243738.713	23 _{5,18} – 23 _{4,19} AE + EA	191.3316	rd
+CH ₃ OCH ₃	243739.900	23 _{5,18} – 23 _{4,19} EE	191.3316	rd
+CH ₃ OCH ₃	243741.087	23 _{5,18} – 23 _{4,19} AA	191.3317	rd
CH ₃ OCH ₃	244508.305	23 _{2,22} – 23 _{1,23} EE	167.9316	rd
+CH ₃ OCH ₃	244512.709	23 _{2,22} – 23 _{1,23} AA	167.9314	rd
CH ₃ OCHO	214782.311	18 _{3,16} – 17 _{3,15} E	66.4186	rd
CH ₃ OCHO	216109.780	19 _{2,18} – 18 _{2,17} E	68.7869	map
+DCO ⁺	216112.580	3 _{0,0} – 2 _{0,0}	7.2089	
CH ₃ OCHO	216966.246	20 – 19	70.2584	¹ , map
CH ₃ OCHO	220166.809	17 _{4,13} – 16 _{4,12} E	64.3503	rd
CH ₃ OCHO	221693.077	10 _{4,6} – 9 _{3,7} E	22.6450	rd
CH ₃ OCHO	222421.356	18 _{8,10} – 17 _{8,9} E	92.3441	rd
CH ₃ OCHO	222657.320	8 _{5,3} – 7 _{4,3} E	18.8854	rd
CH ₃ OCHO	223162.722	18 _{7,11} – 17 _{7,10} A	85.4975	rd
CH ₃ OCHO	225855.505	6 _{6,1} – 5 _{5,1} E	17.6920	rd
CH ₃ OCHO	227019.516	19 _{2,17} – 18 _{2,16} E	73.4502	rd
CH ₃ OCHO	227563.734	21 – 20	77.4957	¹ , map
CH ₃ OCHO	228628.792	18 _{5,13} – 17 _{5,12} E	74.9364	rd
CH ₃ OCHO	229405.001	18 _{3,15} – 17 _{3,14} E	69.3158	rd
CH ₃ OCHO	229420.343	18 _{3,15} – 17 _{3,14} A	69.3100	rd
CH ₃ OCHO	233226.782	19 _{4,16} – 18 _{4,15} A	77.8820	rd
CH ₃ OCHO	233845.126	19 _{11,8} – 18 _{11,7} E	125.9196	rd
CH ₃ OCHO	235029.886	19 _{8,11} – 18 _{8,10} E	99.7633	rd

Molecule	Frequency (MHz)	Transition	Low level energy (cm ⁻¹)	Comments
CH ₃ OCHO	235263.315	9 _{9,0} – 9 _{8,1} <i>A</i>	47.9776	rd
CH ₃ OCHO	235844.542	19 _{7,13} – 18 _{7,12} <i>A</i>	92.9388	rd
CH ₃ OCHO	235865.878	19 _{7,13} – 18 _{7,12} <i>E</i>	92.9388	rd
CH ₃ OCHO	236365.562	20 _{3,18} – 19 _{3,17} <i>A</i>	81.1013	rd
CH ₃ OCHO	236743.645	19 _{5,15} – 18 _{5,14} <i>E</i>	82.1900	rd
CH ₃ OCHO	236800.513	19 _{6,14} – 18 _{6,13} <i>E</i>	87.1016	rd
CH ₃ OCHO	236810.327	19 _{6,14} – 18 _{6,13} <i>A</i>	87.0979	rd
CH ₃ OCHO	237398.615	21 _{2,20} – 20 _{1,19} <i>A</i>	83.5457	rd
CH ₃ OCHO	237807.577	19 _{6,13} – 18 _{6,12} <i>E</i>	87.1428	rd
CH ₃ OCHO	237829.829	19 _{6,13} – 18 _{6,12} <i>A</i>	87.1385	rd
CH ₃ OCHO	238157.297	22 – 21	85.0863	¹ ,map
CH ₃ OCHO	240021.129	19 _{3,16} – 18 _{3,15} <i>E</i>	76.9679	rd
CH ₃ OCHO	242871.513	19 _{5,14} – 18 _{5,13} <i>E</i>	82.5627	rd
CH ₃ OCHO	242896.022	19 _{5,14} – 18 _{5,13} <i>A</i>	82.5584	rd
CH ₃ OCHO	244580.313	20 _{4,17} – 19 _{4,16} <i>E</i>	85.6670	rd
CH ₃ OCHO	246891.590	19 _{4,15} – 18 _{4,14} <i>E</i>	79.4914	rd
CH ₃ OCHO	249047.435	20 _{5,16} – 19 _{5,15} <i>A</i>	90.0826	rd
CH ₃ OH	211803.245	16 _{2,15} – 15 _{1,14} <i>A</i> [–] <i>ν_t</i> = 1	419.2430	rd
CH ₃ OH	213159.369	20 _{–4,17} – 19 _{–5,14} <i>E</i>	392.4940	rd
CH ₃ OH	213377.521	13 _{6,8} – 14 _{5,10} <i>E</i>	263.8890	rd
CH ₃ OH	213427.061	1 ₁ – 0 ₀ <i>E</i>	9.1220	map, rd
CH ₃ OH	215302.205	6 _{1,6} – 7 _{2,5} <i>A</i> ⁺ <i>ν_t</i> = 1	252.6430	rd
CH ₃ OH	216945.559	5 _{1,4} – 4 _{2,2} <i>E</i>	31.5960	rd
CH ₃ OH	217299.205	6 ₁ – 7 ₂ <i>A</i> [–] <i>ν_t</i> = 1	252.6437	map, rd
CH ₃ OH	217886.39	20 _{1,19} – 20 _{0,20} <i>E</i>	346.0730	rd
CH ₃ OH	218440.063	4 ₂ – 3 ₁ <i>E</i>	24.3097	map, rd
CH ₃ OH	220078.561	8 ₀ – 7 ₁ <i>E</i>	59.8092	map, rd
CH ₃ OH	222722.796	16 _{2,14} – 15 _{1,15} <i>A</i> ⁺ <i>ν_t</i> = 1	418.8610	rd
CH ₃ OH	224699.714	20 _{–2,19} – 19 _{–3,17} <i>E</i>	349.9350	rd
CH ₃ OH	227094.600	21 _{1,20} – 21 _{0,21} <i>E</i>	379.6110	rd
CH ₃ OH	227814.528	16 ₁ – 15 ₂ <i>A</i> ⁺	219.8440	map, rd
CH ₃ OH	229589.056	15 ₄ – 16 ₃ <i>E</i>	252.5906	map, rd
CH ₃ OH	229758.811	8 _{–1,8} – 7 _{0,7} <i>E</i>	54.2660	rd
CH ₃ OH	229939.180	19 _{5,14} – 20 _{4,17} <i>A</i> [–]	394.4770	rd
CH ₃ OH	230027.002	3 _{–2,2} – 4 _{–1,4} <i>E</i>	20.0090	rd
CH ₃ OH	231281.110	10 ₂ – 9 ₃ <i>A</i> [–]	107.2083	map, rd
CH ₃ OH	232418.571	10 _{2,8} – 9 _{3,7} <i>A</i> ⁺	107.2080	rd
CH ₃ OH	232783.591	18 _{3,16} – 17 _{4,13} <i>A</i> ⁺	302.5920	rd
CH ₃ OH	232945.797	10 _{–3} – 11 _{–2} <i>E</i>	124.5436	map, rd
CH ₃ OH	233795.799	18 _{3,15} – 17 _{4,14} <i>A</i> [–]	302.5920	rd
CH ₃ OH	234683.370	4 ₂ – 5 ₁ <i>A</i> [–]	34.5156	map, rd
CH ₃ OH	234698.519	5 _{–4} – 6 _{–3} <i>E</i>	77.4675	map, rd
CH ₃ OH	236936.089	14 ₁ – 13 ₂ <i>A</i> [–]	172.9481	map, rd
CH ₃ OH	237129.23	22 _{1,21} – 22 _{0,22} <i>E</i>	414.7270	rd
CH ₃ OH	239746.219	5 ₁ – 4 ₁ <i>A</i> ⁺	26.1012	map, rd
CH ₃ OH	240241.490	5 ₃ – 6 ₂ <i>E</i>	49.3488	map, rd
CH ₃ OH	240960.557	5 ₁ – 4 ₁ <i>A</i> ⁺ , <i>ν_t</i> = 1	242.1426	map
CH ₃ OH	241206.035	5 ₀ – 4 ₀ <i>E</i> , <i>ν_t</i> = 1	225.0053	map
CH ₃ OH	241238.108	5 _{–1,4} – 4 _{–1,3} <i>E</i> <i>ν_t</i> = 1	303.4060	rd
CH ₃ OH	241267.822	5 _{0,5} – 4 _{0,4} <i>A</i> ⁺ <i>ν_t</i> = 1	310.5470	rd
CH ₃ OH	241364.12	5 _{1,4} – 4 _{1,3} <i>A</i> [–] <i>ν_t</i> = 2	490.6630	rd
CH ₃ OH	241441.265	5 _{1,4} – 4 _{1,3} <i>A</i> [–] <i>ν_t</i> = 1	242.1750	rd
CH ₃ OH	241700.159	5 ₀ – 4 ₀ <i>E</i>	25.2542	map

Molecule	Frequency (MHz)	Transition	Low level energy (cm ⁻¹)	Comments
CH ₃ OH	241767.234	5 ₋₁ – 4 ₋₁ E	20.0091	map
CH ₃ OH	241791.352	5 ₀ – 4 ₀ A ⁺	16.1335	map, rd
CH ₃ OH	241806.525	5 ₄ – 4 ₄ A ⁺	71.9750	map
		+5 ₄ – 4 ₄ A ⁻		map
CH ₃ OH	241813.255	5 ₋₄ – 4 ₋₄ E	77.2302	map
CH ₃ OH	241832.718	5 ₃ – 4 ₃ A ⁺	50.7463	map
		+5 ₃ – 4 ₃ A ⁻		map
CH ₃ OH	241843.604	5 ₃ – 4 ₃ E	49.2953	map
CH ₃ OH	241852.299	5 ₋₃ – 4 ₋₃ E	59.7198	map
CH ₃ OH	241879.025	5 ₁ – 4 ₁ E	30.7644	map
CH ₃ OH	241887.674	5 ₂ – 4 ₂ A ⁺	42.3450	map
CH ₃ OH	241904.147	5 ₂ – 4 ₂ E	34.1368	map
+CH ₃ OH	241904.643	5 ₋₂ – 4 ₋₂ E	31.5961	map
CH ₃ OH	242446.084	14 ₋₁ – 13 ₋₂ E	164.9296	map, rd
CH ₃ OH	243413.43	23 _{3,20} – 23 _{2,21} A ⁻⁺	471.5150	rd
CH ₃ OH	243915.788	5 ₁ – 4 ₁ A ⁻	26.3795	map, rd
CH ₃ OH	244330.987	22 _{3,19} – 22 _{2,20} A ⁻⁺	434.4160	rd
CH ₃ OH	244338.004	9 _{1,9} – 8 _{0,8} E $\nu_t = 1$	266.8380	rd
CH ₃ OH	245223.465	21 _{3,18} – 22 _{2,19} A ⁻⁺	398.9280	rd
CH ₃ OH	246074.914	20 _{3,17} – 20 _{2,18} A ⁻⁺	365.0510	rd
CH ₃ OH	246873.503	19 _{3,16} – 19 _{2,17} A ⁻⁺	332.7850	rd
CH ₃ OH	247161.950	16 ₂ – 15 ₃ E	226.7747	map, rd
CH ₃ OH	247228.587	4 ₂ – 5 ₁ A ⁺	34.0983	map, rd
CH ₃ OH	247611.037	18 _{3,15} – 18 _{2,16} A ⁻⁺	302.1310	rd
CH ₃ OH	247840.224	12 _{-2,10} – 13 _{-3,10} E $\nu_t = 1$	370.6090	rd
CH ₃ OH	248282.424	17 ₃ – 17 ₂ A ⁻⁺	273.0892	map
CH ₃ OH	248885.468	16 ₃ – 16 ₂ A ⁻⁺	245.6602	map, rd
CH ₃ OH	249192.864	16 _{-3,14} – 15 _{-4,12} E	254.6040	rd
CH ₃ OH	249419.924	15 ₃ – 15 ₂ A ⁻⁺	219.8440	map, rd
CH ₃ OH	249443.402	7 _{4,4} – 8 _{3,5} A ⁻	92.6910	rd
CH ₃ OH	249451.885	7 _{4,3} – 8 _{3,6} A ⁺	92.6900	rd
CN	226359.987	2 – 1 J = 3/2 – 3/2 F = 5/2 – 5/2	3.7857	map
CN	226632.190	2 – 1 J = 3/2 – 1/2 F = 3/2 – 3/2	3.7757	map
CN	226659.575	2 – 1 J = 3/2 – 1/2 F = 5/2 – 3/2	3.7757	map
CN	226679.382	2 – 1 J = 3/2 – 1/2 F = 3/2 – 1/2	3.7741	map
CN	226875.897	2 – 1 J = 5/2 – 3/2 F = 3/2 – 1/2	3.7866	map
CS	244935.644	5 – 4	16.3411	map
H ₂ ¹³ CO	219908.525	3 _{1,2} – 2 _{1,1}	15.5579	map
H ₂ CO	211211.468	3 _{1,3} – 2 _{1,2}	15.2369	map, rd
H ₂ CO	216568.668	9 _{1,8} – 9 _{1,9}	113.7050	rd
H ₂ CO	218222.192	3 _{0,3} – 2 _{0,2}	7.2864	map, rd
H ₂ CO	218475.632	3 _{2,2} – 2 _{2,1}	40.0402	map, rd
H ₂ CO	218760.066	3 _{2,1} – 2 _{2,0}	40.0426	map, rd
H ₂ CO	225697.775	3 _{1,2} – 2 _{1,1}	15.7202	map, rd
H ₂ CS	236726.770	7 _{1,7} – 6 _{1,6}	32.8599	map
H ₂ CS	240266.320	7 _{0,7} – 6 _{0,6}	24.0546	map
H ₂ CS	244047.840	7 _{1,6} – 6 _{1,5}	33.5928	map
H ₂ S	216710.435	2 _{2,0} – 2 _{1,1}	51.1402	map

Molecule	Frequency (MHz)	Transition	Low level energy (cm ⁻¹)	Comments
HCCCN	236512.777	26 – 25	98.6235	map
HCCCN	245606.308	27 – 26	106.5127	map
HCOOH	220037.960	10 _{0,10} – 9 _{0,9}	33.4039	rd
HCOOH	223915.560	10 _{2,9} – 9 _{2,8}	42.5246	rd
HCOOH	225085.440	10 _{4,7} – 9 _{4,6}	69.1174	rd
HCOOH	225091.210	10 _{4,6} – 9 _{4,5}	69.1175	rd
HCOOH	225512.540	10 _{3,7} – 9 _{3,6}	53.6767	rd
HCOOH	228544.070	10 _{2,8} – 9 _{2,7}	42.8481	rd
HCOOH	231505.590	10 _{1,9} – 9 _{1,8}	37.0844	rd
HCOOH	236717.326	11 _{1,11} – 10 _{1,10}	41.8215	map, rd
HCOOH	241146.200	11 _{0,11} – 10 _{0,10}	40.7435	rd
HCOOH	246106.087	11 _{2,10} – 10 _{2,9}	49.9937	map, rd
HCOOH	247514.120	11 _{*,6} – 10 _{*,5}	96.4903	rd
HCS ⁺	213360.530	5 – 4	14.2343	map
HNCO	218981.031	10 _{1,10} – 9 _{1,9}	62.9493	map, rd
HNCO	219656.805	10 _{3,7} – 9 _{3,6} +10 _{3,8} – 9 _{3,7}	303.6759	rd
HNCO	219733.824	10 _{2,9} – 9 _{2,8}	153.2967	rd
HNCO	219798.247	10 _{0,10} – 9 _{0,9}	32.9940	map, rd
HNCO	220585.200	10 _{1,9} – 9 _{1,8}	63.1900	map, rd
HNCO	231873.255	28 _{1,28} – 29 _{0,29}	318.8428	rd
HNCO	240875.856	11 _{1,11} – 10 _{1,10}	70.2537	map, rd
HNCO	241774.037	11 _{0,11} – 10 _{0,10}	40.3257	rd
HNCO	242639.705	11 _{0,10} – 10 _{0,9}	70.5480	rd
OCS	231060.983	19 – 18	69.3719	map
OCS	243218.040	20 – 19	77.0793	map
SO	215220.653	<i>N, J = 5, 5 – 4, 4</i>	23.4748	map
SO	219949.442	<i>N, J = 5, 6 – 4, 5</i>	16.9790	map
³⁴ SO	215839.920	<i>N, J = 5, 6 – 4, 5</i>	16.6981	map
SO ₂	221965.210	11 _{1,11} – 10 _{0,10}	34.5495	map
SO ₂	224264.811	20 _{2,16} – 19 _{3,17}	136.9168	map
SO ₂	225153.702	13 _{2,12} – 13 _{1,13}	57.1170	map
SO ₂	226300.027	14 _{3,11} – 14 _{2,12}	75.1496	map
SO ₂	235151.720	4 _{2,2} – 3 _{1,3}	5.3820	map
SO ₂	236216.685	16 _{1,15} – 15 _{2,14}	82.9373	map
SO ₂	237068.870	12 _{3,9} – 12 _{2,10}	57.3978	map
SO ₂	241615.798	5 _{2,4} – 4 _{1,3}	8.3356	map
SO ₂	244254.218	14 _{0,14} – 13 _{1,13}	57.1170	map
SO ₂	245563.423	10 _{3,7} – 10 _{2,8}	42.3467	map

¹–blend of several CH₃OCHO transitions.